Biophysical Journal
Article

Biophysical Society

An integrate-and-fire approach to Ca^{2+} signaling. Part I: Renewal model

Lukas Ramlow,[1,2,*] Martin Falcke,[2,3] and Benjamin Lindner[1,2]
[1]Bernstein Center for Computational Neuroscience Berlin, Berlin, Germany; [2]Physics Department of Humboldt University Berlin, Berlin, Germany; and [3]Max Delbrück Center for Molecular Medicine, Berlin, Germany

ABSTRACT In computational neuroscience integrate-and-fire models capture the spike generation by a subthreshold dynamics supplemented by a simple fire-and-reset rule; they allow for a numerically efficient and analytically tractable description of stochastic single cell as well as network dynamics. Stochastic spiking is also a prominent feature of Ca^{2+} signaling which suggests to adopt the integrate-and-fire approach for this fundamental biophysical process. The model introduced here consists of two components describing 1) activity of clusters of inositol-trisphosphate receptor channels and 2) dynamics of the global Ca^{2+} concentrations in the cytosol. The cluster dynamics is given in terms of a cyclic Markov chain, capturing the puff, i.e., the punctuated release of Ca^{2+} from intracellular stores. The cytosolic Ca^{2+} concentration is described by an integrate-and-fire dynamics driven by the puff current. For the cyclic Markov chain we derive expressions for the statistics of the interpuff interval, the single-puff strength and the puff current assuming constant cytosolic Ca^{2+}. The latter condition is often well approximated because cytosolic Ca^{2+} varies much slower than the cluster activity does. Furthermore, because the detailed two-component model is numerically expensive to simulate and difficult to treat analytically, we develop an analytical framework to approximate the driving puff current of the stochastic cytosolic Ca^{2+} dynamics by a temporally uncorrelated Gaussian noise. This approximation reduces our two-component system to an integrate-and-fire model with a nonlinear drift function and a multiplicative Gaussian white noise, a model that is known to generate a renewal spike train, i.e., a point process with statistically independent interspike intervals. The model allows for fast numerical simulations, permits to derive analytical expressions for the rate of Ca^{2+} spiking and the coefficient of variation of the interspike interval, and to approximate the interspike interval density and the spike train power spectrum. Comparison of these statistics to experimental data is discussed.

SIGNIFICANCE The concentration of intracellular Ca^{2+} controls many cellular processes and exhibits prominent pulses (spikes). The timing of these spikes is rather irregular due to an interplay of the intracellular Ca^{2+} dynamics with the random opening and closing of Ca^{2+} channel clusters in the membrane of the endoplasmic reticulum. Here, we propose a mathematical model for the random (stochastic) spike generation that incorporates these two components. Since cluster activity is often very fast compared with the change in Ca^{2+} concentration, we can further reduce our two-component model resulting in a simplified stochastic model that can be rapidly simulated. Moreover, the simpler model allows for analytical approximations of the statistics of interest, which can be compared with those of experimental data.

INTRODUCTION

Calcium (Ca^{2+}) is a ubiquitous intracellular messenger that regulates many cellular processes, ranging from muscle contraction and relaxation over neurotransmitter secretion in synapses to fertilization and apoptosis (1–5). To utilize Ca^{2+} signaling effectively, cells maintain a extraordinary low resting cytosolic Ca^{2+} concentration ($[Ca^{2+}]_i < 100$ nM) much smaller than the extracellular Ca^{2+} concentration ($[Ca^{2+}]_{ex} \approx 1$ nM) (6). The associated large gradient is maintained by a number of pumps that transport Ca^{2+} from the cytosol into the extracellular medium but also into the endoplasmic reticulum (ER) serving as an intracellular Ca^{2+} store with a lumenal concentration three to four orders of magnitude larger than the cytosolic resting concentration. Release of Ca^{2+} from the ER through the designated inositol trisphosphate receptor (IP_3R) channel and controlled by the second messenger inositol trisphosphate (IP_3) causes

Submitted October 19, 2022, and accepted for publication January 6, 2023.
*Correspondence: lukas.ramlow@bccn-berlin.de
https://doi.org/10.1016/j.bpj.2023.01.007

short pulse-like deflections of the cytosolic Ca^{2+} concentration called spikes.

Ca^{2+} spiking is a stochastic process (7–17). The sequence of spike times is strongly affected by randomness due to the finite-size noise of the involved molecules as well as cooperativity of the ion channels (see below). Theoretical understanding of Ca^{2+} signaling requires stochastic models that take these fluctuations into account. Such models exist (9,18–22) but so far do not focus on the spike statistics as a point process. In computational neuroscience an important model class for the description of a stochastic point process, associated with the spiking in the membrane voltage of neurons, is the integrate-and-fire (IF) neuron (23–26). Here, we attempt to adopt this successful framework to the problem of Ca^{2+} spiking; for a recent discussion of the similarities and differences between calcium and neural spiking (see, e.g., (27)).

The defining idea of an IF approach is to model the dynamics of the spiking variable (in computational neuroscience the membrane voltage) only up to its spike-triggering threshold, and to replace the stereotypical spike by a fire-and-reset rule. The most important output of such a model is the sequence of spike times t_i or, equivalently, the spike train:

$$z(t) = \sum_i \delta(t - t_i), \tag{1}$$

a sum of Dirac delta functions $\delta(\cdot)$ at the spike times. IF models are successful in reproducing and predicting the spike times of detailed neuron models (26) and real neurons (28,29) alike and are analytically tractable in many situations (see, e.g., (30–35)).

Crucial for the applicability of IF models is a reliable spike generation once the threshold is crossed. This in turn is implemented by a positive feedback mechanism, based on voltage-gated ion channels that are selective for Na^+ ions. Superthreshold depolarization of the voltage opens Na^+ channels triggering a Na^+-flux into the cell, that leads to a further depolarization of the voltage and activates even more Na^+ channels and so on. Ca^{2+}-induced Ca^{2+} release, a process in which Ca^{2+} itself promotes the release of Ca^{2+} from the ER, constitutes such a positive feedback mechanism in the context of Ca^{2+} spiking.

The model we propose here consists of two components. The first describes the dynamics of the intracellular Ca^{2+} concentration by means of an IF model. The second captures the release of Ca^{2+} from the ER by the stochastic opening of clusters of IP_3Rs (modeling channel activity by Markovian models has a long tradition, for an overview see (21)). These local releases are called puffs and form the elementary events of global spikes. We describe them by a cyclic Markov chain modeling the number of open channels in a given cluster. The Ca^{2+} puff current through these channels results from the concentration gradient between ER and cytosol. We calculate statistics of the puff strength and interpuff interval (IPI) as well as the noise intensity of the puff current from the Markov chain.

The model for the global intracellular Ca^{2+} concentration is hard to treat analytically because the driving puff current depends on the cytosolic Ca^{2+} concentration itself and possesses complicated statistics. However, because the opening and closing of IP_3R clusters is often fast, we exploit the timescale separation between the fast IP_3-dependent puff current and the remaining slow IP_3-independent Ca^{2+} currents. This allows for a diffusion approximation of the puff current and reduces the two-component model to a one-component IF model with nonlinear drift and Gaussian white noise. This reduced model generates a renewal point process, i.e., all interspike intervals (ISIs) are mutually statistically independent; this is also true to a very good approximation for the original two-component model. The reduced one-component model is analytically tractable and allows to calculate statistics such as the stationary probability density of the subthreshold Ca^{2+} concentration, the firing rate, and the coefficient of variation (CV) of the ISI. We find, that for our model the ISI density is well approximated by an inverse Gaussian distribution which for the generated renewal point process provides a complete description of the spike statistics and allows for an instance to calculate the spike-train power spectrum. We show that the model can reproduce quantitatively statistics of stimulated HEK cells that have been shown to generate renewal spike trains (36).

The paper is organized as follows. We first introduce the two-component model for Ca^{2+} spiking starting with the IF model that governs the dynamics of the subthreshold cytosolic Ca^{2+} concentration. In the following section we introduce the cyclic Markov chain that models the cooperative opening and closing of IP_3R clusters and gives rise to a stochastic Ca^{2+} current that feeds into the cytosolic Ca^{2+} concentration. Before discussing the full two-component model we study the Markov chain for a fixed cytosolic Ca^{2+} concentration and provide exact analytical results for statistics of the puff strength and IPI as well as the mean and noise intensity of the puff current. In the subsequent section we approximate the stochastic puff current by a deterministic mean and Gaussian white noise, based on a timescale separation between the Ca^{2+} currents. This gives rise to a one-component nonlinear Langevin equation with a spike-and-reset rule, that can be treated analytically by means of the associated Fokker-Planck equation (FPE). Finally, we compare statistics of the full two-component model to those of the one-component Langevin approximation and also to stimulated HEK cells. For an overview of the introduced variables and parameters see Table 1.

Two-component model for cytosolic Ca^{2+} and stochastic IP_3R cluster dynamics

Cytosolic Ca^{2+}: IF model

We introduce an IF modeling approach to the repetitive spiking of $[Ca^{2+}]_i$. In such a framework the dynamics of

TABLE 1 Variables and parameters

Symbol	Meaning
$c_i(t)$	cytosolic Ca^{2+} concentration
c_0, c_R, c_T	resting, reset, threshold values of c_i
τ	time constant of c_i dynamics
$j_{puff}(c_i)$	puff current
p	permeability-like parameter
Δc_{er}	concentration difference between cytosol and endoplasmic reticulum
$x_k(t)$	number of open channels in the kth cluster
K	number of cluster
N	number of channels per cluster
M	number of refractory states per cluster
λ_{cls}, λ_{opn}, λ_{ref}	rates of the Markov chain
α, β	Hill coefficient of opening rate
s	stimulation amplitude of IP_3
t_i	spike times
$z(t)$	spike train
T_i	interspike intervals
A_i	puff strength
I_i	interpuff interval

$[Ca^{2+}]_i$ is modeled only over a small part of its physiological range, i.e., up to a certain threshold that is much smaller than the peak concentration during a spike. We assume that over this range the change of the (nondimensional) cytosolic Ca^{2+} concentration c_i (see below Eq. 7) can be described by two currents. The first current $j_{lin} = (c_0 - c_i)/\tau$ gives rise to a stable resting concentration c_0 in the absence of a stimulation and perturbations decay toward this value with a time constant τ. It subsumes all passive and active currents that are independent of IP_3 including leak currents through the ER and cellular membranes as well as ATP-fueled Ca^{2+} pumps (SERCA activity). The second current j_{puff}, the IP_3-dependent puff current, describes the release of Ca^{2+} from the ER by clustered IP_3Rs and also mediates the positive feedback mechanism known as Ca^{2+}-induced Ca^{2+} release. In line with these assumptions, the Parker lab (37,38) has recently shown that the main share of Ca^{2+} released into the cell during the rising phase of a Ca^{2+} spike is due to a punctuated release of Ca^{2+} from clustered IP_3Rs, corresponding to j_{puff} in our model. Furthermore they found that after a spike, when puffs are absent, the return to the resting concentration is well described by an exponential decay with a single time constant τ, corresponding to j_{lin} in our model. The IF model reads:

$$\begin{aligned} \dot{c}_i &= -(c_i - c_0)/\tau + j_{puff}(c_i) \\ \text{if } c_i(t) &= c_T \to t_i = t \text{ and } c_i(t) = c_R \end{aligned} \tag{2}$$

where $c_i(t)$, c_0, c_R and c_T represent the cytosolic, resting, reset and threshold Ca^{2+} concentrations, respectively. The first term on the r.h.s. is the *deterministic* linear current with timescale τ that determines how quickly the resting concentration c_0 is reached in the absence of puffs. The second term is the *stochastic* puff current resulting from the release of Ca^{2+} from the ER by the stochastic opening and closing of clustered IP_3Rs. We describe j_{puff} as:

$$j_{puff}(c_i) = p\Delta c_{er} \sum_{k=1}^{K} x_k(t), \tag{3}$$

where p is a permeability-like parameter, Δc_{er} is the concentration gradient between ER and cytosol, and $x_k(t)$ refers to the number of open channels in the kth of a total of K clusters. The kinetics of $x_k(t)$ are detailed in the following section. Since the Ca^{2+} concentration in the ER is much larger than in the cytosol (5,21), we assume Δc_{er} to be independent of c_i and constant in time. New aspects arising from a dynamic lumenal concentration will be explored in a subsequent publication.

The IF model is completed by a fire-and-reset rule: at each time $t_i = t$ when $c_i(t)$ reaches the threshold c_T, a spike is assumed to occur and c_i is reset to c_R. If we want to include a finite width of the Ca^{2+} spike we could (similarly to what is done in neuroscience) clamp the Ca^{2+} concentration to c_R for an absolute refractory period τ_{abs}. For simplicity we chose in this paper $\tau_{abs} = 0$ and $c_R = c_0$.

The so far described IF component of our model is illustrated in Fig. 1 *B*. The experimental data shown in Fig. 1 *A* can be mimicked by the model if the parameters are chosen accordingly such that the model shows similar values for the stationary mean and CV of the ISI T_i (in the following for stationary statistics of the ISI we will omit the index i); this is further discussed below.

IP_3R clusters: Cyclic Markov model

The number of open channels in each cluster, $x(t)$ (omitting the cluster index k), is modeled by a cyclic Markov chain that is shown in Fig. 2 (*top left*). The model is based on experimentally accessible statistics of the puff strength and IPI. There exists of course a large variety of detailed single IP_3R models upon which a cluster model could be build (39), for instance, the classic De Young-Keizer model (40) or the more recent data-driven models by Gin et al. (41) and Siekmann et al. (42), to name just a few. However, because channels within a cluster are highly cooperative, indicating strong coupling, cluster models derived from single-channel-state schemes are very complex (43,44). Since these complex dynamics result in rather simple waiting time distributions for closed and open cluster states (43,45–47), we follow here a different approach.

For our model each cluster is described by a continuous-time Markov chain $\omega(t)$ with state space $\Omega = [N, \ldots, 1, 0_M, \ldots, 0_1]$ that consists of two subsets $\Omega_N = [N, \ldots, 1]$ and $\Omega_M = [0_M, \ldots, 0_1]$ where the cluster is considered open and closed, respectively (see Fig. 2). The states are labeled according to the number of open channels they represent and we refer to the probability

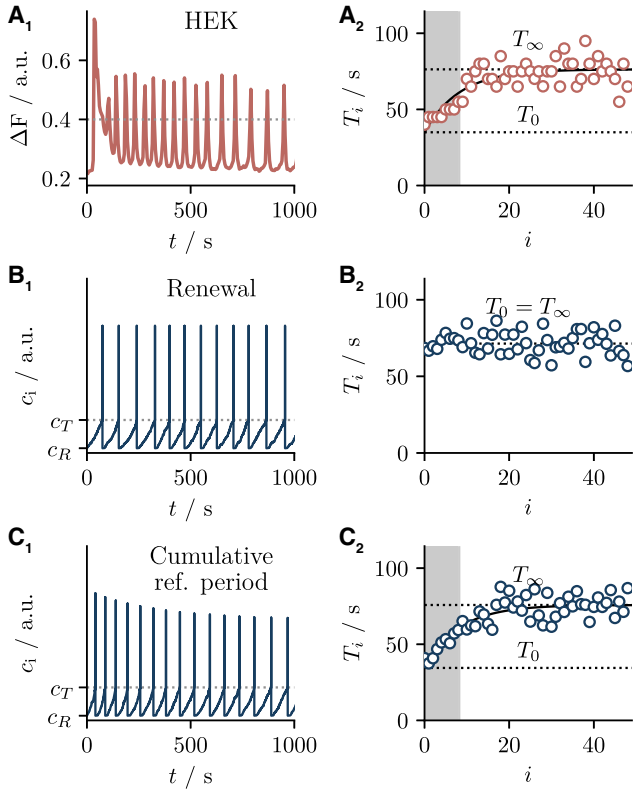

FIGURE 1 An integrate-and-fire approach to Ca^{2+} spiking. (*A–C*) Show experimental data (as described in (10,14)), the renewal model (subject of this paper), and the model with cumulative refractoriness (subject of a forthcoming paper), respectively. (A_1) Shows the time series of the fluorescence signal ΔF proportional to the free cytosolic Ca^{2+} concentration obtained from stimulated HEK cells (a step stimulus with onset at $t = 0$). For each time series, the time of up-crossing a certain threshold (*dotted line*) defines a series of spike time t_1, t_2, t_3, …. (A_2) Shows the corresponding sequence of ISIs $T_i = t_{i+1} - t_i$ over the index i that exhibits a long transient fitted by an exponential function $T_\infty - (T_\infty - T_0)\exp(-i/n_{\mathrm{tr}})$ (*black line*). The initial ISI T_0 and stationary ISI T_∞ according to this fit are shown by dotted lines. The characteristic number n_{tr} is indicated by the gray area. (B_1 and B_2) Show traces of the (nondimensional) cytosolic Ca^{2+} concentration c_i (here i stands for *intracellular*) and the corresponding sequence of ISIs T_i obtained from stochastic simulations of the two-component model Eq. 2 presented in this paper. The model reproduces the stationary mean and CV of the experimental data but does not account for the transient in the ISI sequence. In a follow-up paper we introduce an extension of this model that captures the transient behavior by taking into account the depletion of intracellular Ca^{2+} stores. (C_1 and C_2) Show again traces of the cytosolic Ca^{2+} concentration c_i and the corresponding sequence of ISIs obtained from the extended model that reproduces not only the stationary mean and CV but also the characteristic number n_{tr} and cumulative refractory period $T_\infty - T_0$ of the experimental ISI sequence. To see this figure in color, go online.

that a state ω is occupied by $p(\omega, t)$ or equivalently by the ωth component of a probability vector $\boldsymbol{p}(t)$. The master equation is given by:

$$\frac{d}{dt}\boldsymbol{p}(t) = W\cdot\boldsymbol{p}(t), \tag{4}$$

with the transition rate matrix W:

$$\left(\begin{array}{cccc|ccccc}
-\lambda_{\mathrm{cls}} & & & & & & & & \lambda_{\mathrm{opn}}/N \\
\lambda_{\mathrm{cls}} & \ddots & & & & & & & \vdots \\
 & \ddots & \ddots & & & & & & \vdots \\
 & & \lambda_{\mathrm{cls}} & -\lambda_{\mathrm{cls}} & & & & & \lambda_{\mathrm{opn}}/N \\
\hline
 & & & \lambda_{\mathrm{cls}} & -\lambda_{\mathrm{ref}} & & & & \\
 & & & & \lambda_{\mathrm{ref}} & \ddots & & & \\
 & & & & & \ddots & -\lambda_{\mathrm{ref}} & & \\
 & & & & & & \lambda_{\mathrm{ref}} & -\lambda_{\mathrm{opn}}
\end{array}\right) \tag{5}$$

where each blank entry corresponds to a zero, and the probability vector $\boldsymbol{p}(t)$:

$$(p(N,t) \quad \ldots \quad p(1,t) \quad p(0_M,t) \quad \ldots \quad p(0_1,t))^T \tag{6}$$

Furthermore, we assign to every state ω a natural number as follows:

$$x(\omega) = \begin{cases} n, \text{for } \omega \in \Omega_N, \\ 0, \text{for } \omega \in \Omega_M. \end{cases}$$

Here, n is the number of channels that are currently open and corresponds to the label of the state, for instance, $x(\omega = 3) = 3$. The corresponding random process $x(t)$ hence represents the number of open channels at time t and enters the Ca^{2+} dynamics according to Eq. 3. The transition rate matrix W consists of four submatrices that arise due to the classification of the state space into sets of open and closed states. The shapes of the submatrices and their biophysical rationales are described in the following, starting with the top right submatrix and continuing counterclockwise. The first three submatrices determine statistics of the puff (see Fig. 2 *A*), in particular the puff strength A, defined as the integrated Ca^{2+} current during a single puff, while the fourth submatrix determines statistics of the time between two successive puffs, the IPI I (see Fig. 2 *B*).

The top-right $N \times M$ submatrix captures transitions from the closed state $\omega = 0_1$ to the open states and thus the opening of the cluster. Biophysically the firing of a puff is a highly cooperative event triggered by the opening of a single channel which greatly increases the *local* Ca^{2+} concentration. This in turn increases the open probability (48) of the remaining channels in the same cluster and causes a certain, uniformly distributed number of them to respond, i.e., to open as well (49,50). In our model we consider this response to be instantaneous so that the passage from $\omega = 0_1$ (closed) to any number of open channels $\omega = n_0$ (open) is described by single transition. The total escape rate from 0_1, λ_{opn}, depends linearly on the cluster size N, which has been confirmed experimentally (51) and reflects the idea that the opening of any channel can serve as a puff trigger (see Eq. 7). Furthermore, in line with experimental findings (50), we assume that the

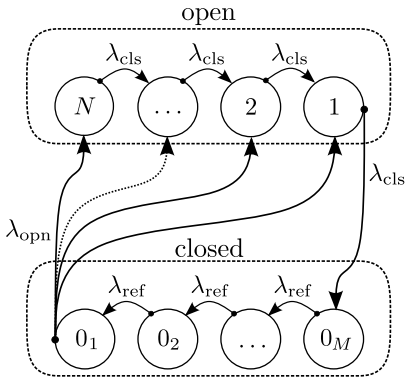

Parameter	Value
N	5
M	3
λ_{cls}	$50\,s^{-1}$
λ_{ref}	$20\,s^{-1}$
$\lambda_{opn}(c_i = c_R, s = 1, N = 5)$	$0.5\,s^{-1}$
α	3.0
β	3.0
s	1.0

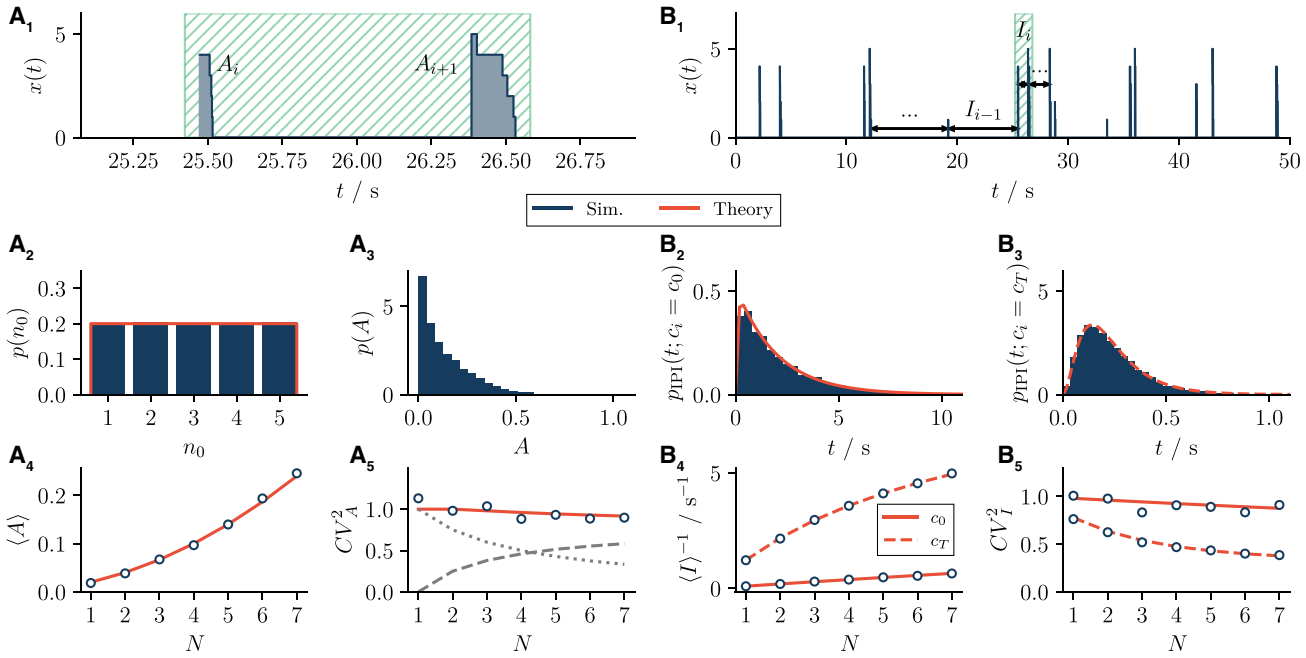

FIGURE 2 Kinetic model of an IP_3R cluster for fixed cytosolic Ca^{2+} and its key statistics. The upper left panel illustrates the cyclic Markov chain that describes the dynamics of a cluster with N open and M closed states. The states are labeled to indicate the number of open channels, captured by the process $x(t) \in [N, \ldots 0]$ that enters the dynamics of the cytosolic Ca^{2+} concentration according to Eqs. 2 and 3. In our model, a puff is initiated whenever there is a transition from the closed state $\omega = 0_1$ to any open state, and ends when the last open state $\omega = 1$ is exited. The IPI is the time between two puffs and corresponds to the time from entering the first closed state $\omega = 0_M$ to leaving the last closed state $\omega = 0_1$. Model parameters are shown in the upper right table. (*A*) Shows statistics of the puff strength A, i.e., the integrated Ca^{2+} current during a single puff. (*B*) Shows statistics of the IPI I. In (A_1) two exemplary puffs with strength A_i and A_{i+1} are shown. (A_2 and A_3) Show the distributions of number of responding channels $p(n_0)$ and puff strength $p(A)$. The former is uniformly distributed by construction. The resulting mean puff strength is a quadratic function of the number of channels N as shown in (A_4). The variability of the puff strength quantified by the (*squared*) coefficient of variation CV_A^2 is bound between 1 and 0.8 as shown in (A_5). This strong variability stems from the stochasticity of the number of responding channels. Gray lines indicate the contribution of $\langle \mathrm{Var}(A|n_0)\rangle / \langle A\rangle^2$ (*dotted*) and $\mathrm{Var}(\langle A|n_0\rangle) / \langle A\rangle^2$ (*dashed*) to the total CV_A^2. In (B_1) an exemplary sequence of IPIs is shown. The IPI distributions at the resting and threshold Ca^{2+} concentrations are shown in (B_2 and B_3), respectively. In each case the distribution possesses a small refractory period determined by the number of refractory states $M - 1$ and the c_i-dependent ratio $\lambda_{opn}/\lambda_{ref}$. The inverse of the mean IPI as a function of the cluster size N is shown in (B_4). For small Ca^{2+} concentrations, close to the resting concentration c_0, the mean IPI is mainly determined by the opening rate that in turn depends linearly on N (Eq. 7), so that $\langle I\rangle^{-1} \propto N$. In contrast, for larger concentrations close to the threshold c_T we observe a somewhat nonlinear shape. The CV_I^2 shown in (B_5) decreases with N and saturates at $1/(M - 1)$. How quickly this limit is approached depends again on $\lambda_{opn}/\lambda_{ref}$ and hence on c_i. To see this figure in color, go online.

corresponding efflux of probability splits equally between all open states, so that the transition rate to a particular open state is λ_{opn}/N. Indeed, as seen in Fig. 2 A_2, the probability for the initial number of open channels in a puff, referred to as the number of responding channels n_0 in the following, is uniformly distributed over the N states.

Once a puff is initiated, the channels close successively according to the top-left $N \times N$ (and bottom-left $M \times N$)

submatrix. Intuitively, one could assume that the channels in a cluster close independently and that the closing rate of the cluster therefore depends linearly on the number of channels n that are currently open. However, Wiltgen et al. (52) have shown that the mean dwell time, the inverse of the closing rate, is largely independent of n indicating that channels do not close independently, but the details of this process are poorly understood. Accordingly, in our model we describe the transition from $\omega = n$ to $\omega = n - 1$ by a fixed closing rate λ_{cls} that is independent of n; an example of the corresponding staircase-like shape of the puff is shown Fig. 2 *A*$_1$. The bottom-left $M \times N$ submatrix, containing only a single entry, describes the closing of the last channel, i.e., transitions from $\omega = 1$ to $\omega = 0_M$.

The bottom-right $M \times M$ submatrix determines statistics of the IPI. Experimentally, it is known that IPIs are highly stochastic but display a (small) refractory period (45,51). The latter can be understood by a negative feedback emerging during the opening of the channel: the local Ca^{2+} concentration in channel proximity attains very large values within microseconds upon channel opening (53) and, after closing of the channel, reduces the probability of immediate reopening for a relative refractory period (48,54). While this feedback is a subject of ongoing discussion, even studies which consider such feedback unlikely come to the conclusion that the IP_3R has more than one closed state (55). IPIs can thus not be modeled by a single transition that would result in an exponential IPI distribution. We introduce a number of refractory states which have to be traversed after a puff was fired before a new puff can be initiated. In detail, the first $M - 1$ closed states have to be traversed with transition rates λ_{ref} before the cluster can open again with the respective opening rate λ_{opn}. At this point, upon reaching the state $\omega = 0_1$, the cycle starts anew with the opening of the cluster captured by the top-right submatrix.

Finally, to complete the model, we state our assumption about the Ca^{2+} and IP_3 dependence of the rates. Unfortunately, an extraction of these rates from experimental data is, to the best of our knowledge, not feasible—a quantitative study that relates puff activity to $[Ca^{2+}]_i$ is missing. For a lack of direct measurements, we choose the open rate's λ_{opn} Ca^{2+} dependence in analogy to the biphasic Ca^{2+} dependence of an individual channel's open probability, usually described by a combination of Hill equations (48,56,57). Since we utilize an IF modeling approach, we are only interested in cluster activity during the rising phase of the Ca^{2+} spike and do not include a term that captures the decrease of the rates at high concentrations. We choose:

$$\lambda_{\mathrm{opn}}(c_{\mathrm{i}}) = N\widehat{\lambda}_{\mathrm{opn}} \frac{c_{\mathrm{i}}^{\alpha}}{1 + c_{\mathrm{i}}^{\alpha}} \frac{s^{\beta}}{1 + s^{\beta}}, \tag{7}$$

where $c_{\mathrm{i}} = [Ca^{2+}]_i/K_{\mathrm{act}}$ and $s = [IP_3]/K_{\mathrm{stim}}$ refer to the cytosolic Ca^{2+} and IP_3 concentration relative to their dissociation constants K_{act} and K_{stim} at which the rates attain half of their maximal value.

The remaining rates of our model λ_{ref}, λ_{cls} do not depend on Ca^{2+} nor on IP_3. The rationale for this choice is a follows: the time for a single channel to be open was shown to be largely independent of Ca^{2+} (56), hence it is plausible that the rate λ_{cls} is unaffected. Furthermore, as discussed above, the local Ca^{2+} concentration after a puff, i.e., during passage of the refractory states, bears little relation to the global Ca^{2+} concentration and thus the rates in the refractory states λ_{ref} may be assumed to be independent of Ca^{2+}. In conclusion we simply assume:

$$\begin{aligned} \lambda_{\mathrm{ref}} &= \text{constant}, \\ \lambda_{\mathrm{cls}} &= \text{constant}. \end{aligned} \tag{8}$$

The resulting open probability of a single cluster is given by:

$$\begin{aligned} p_{\mathrm{opn}}(c_{\mathrm{i}}) &= \frac{\tau_{\mathrm{opn}}}{\tau_{\mathrm{tot}}(c_{\mathrm{i}})} = \frac{\tau_{\mathrm{opn}}}{\tau_{\mathrm{opn}} + \tau_{\mathrm{cls}}(c_{\mathrm{i}})} \\ &= \frac{\dfrac{N+1}{2\lambda_{\mathrm{cls}}}}{\dfrac{N+1}{2\lambda_{\mathrm{cls}}} + \dfrac{M-1}{\lambda_{\mathrm{ref}}} + \dfrac{1}{\lambda_{\mathrm{opn}}(c_{\mathrm{i}})}}, \end{aligned} \tag{9}$$

where $\tau_{\mathrm{opn}} = \sum_{n_0=1}^{N} n_0/(N\lambda_{\mathrm{cls}})$ and $\tau_{\mathrm{cls}} = (M-1)/\lambda_{\mathrm{ref}} + 1/\lambda_{\mathrm{opn}}$ are the mean residence times in the open and closed states, respectively, and $\tau_{\mathrm{tot}} = \tau_{\mathrm{opn}} + \tau_{\mathrm{cls}}$ is the total mean period of the cyclic Markov chain. We note that, τ_{cls} corresponds to the mean IPI and τ_{opn} is the mean puff duration. The resulting open probability and the mean times are shown in Fig. 3 as functions of c_{i}. We indicate by the gray area the c_{i} range that is inaccessible in our IF framework, which does not capture the spike generation itself but only the signal- and noise-dependent subthreshold dynamics. To make a connection to works that cover the full range, we also show a modified open probability with the full biphasic c_{i} dependence obtained by multiplying the opening rate in Eq. 7 by a factor $k^{\alpha}/(k^{\alpha} + c_{\mathrm{i}}^{\alpha})$ with $k = K_{\mathrm{inh}}/K_{\mathrm{act}}$. It becomes apparent, that there is no effect of this inhibitory term for the subthreshold c_{i} relevant in our model.

Equation 2 for the IF component and Eq. 4 for the K clusters of IP_3R channels constitute the complete model that can be simulated by the typical integration schemes for differential and master equations.

RESULTS

Statistics of a single IP_3R cluster for fixed Ca^{2+}: Analytical results

Here, we calculate statistics of the puff strength A and IPI I. Because the Ca^{2+} concentration usually changes very slowly compared with the cluster activity, we assume that

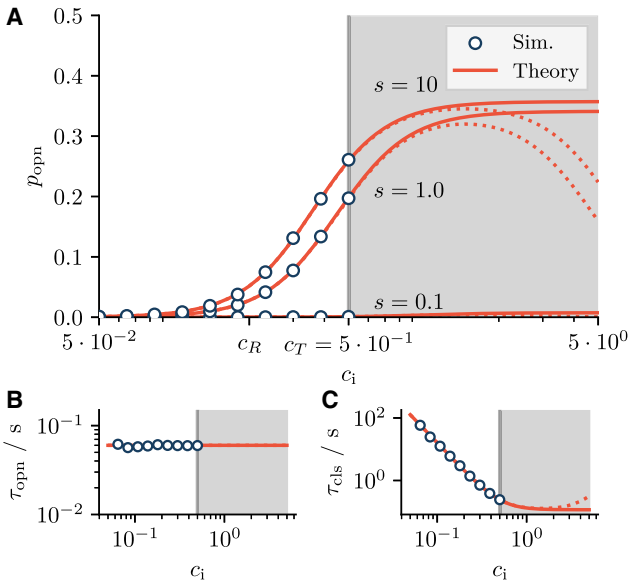

FIGURE 3 Open probability and dwell times of an IP_3R cluster for fixed cytosolic Ca^{2+}. (*A*) Shows the open probability p_{opn} of a single cluster over the relative Ca^{2+} concentration c_i for a weak ($s = 0.1$), intermediate ($s = 1.0$), and strong ($s = 10$) stimulation. The threshold of Ca^{2+} spiking is indicated by a gray line and separates sub-from suprathreshold concentrations (*gray area* indicating c_i values that are not modeled). Theoretical predictions of p_{opn} according to Eq. 9 (*solid red lines*) are confirmed by simulation results (*blue circles*). (*B*) Shows the mean dwell times in the open states that is independent of c_i because the involved rate λ_{cls} is independent of c_i. (*C*) Shows the mean dwell time in the closed states (τ_{cls}) that depends on c_i through λ_{opn}. Hence, the increase of p_{opn} with c_i (see (*A*)) stems from a decrease of τ_{cls}. To make a relation to the existing literature, we show the open probability (and mean dwell times) with a true biphasic c_i dependence of the opening rate λ_{opn} by a dotted line. To this end we multiply the opening rate as given in Eq. 7 by an additional term $k^\alpha/(k^\alpha + c_i^\alpha)$ that inhibits cluster activity at high concentrations $c_i > c_T$. The parameter $k = K_{inh}/K_{act}$ represents the ratio between the dissociation constants of activation and inhibition Ca^{2+} and was set to $k = 10$. The additional term affects the cluster dynamic only at high Ca^{2+} concentrations that are of no interest in an IF framework. Parameters are chosen according to Fig. 2. To see this figure in color, go online.

c_i is fixed. In this case and I are fully independent and can be calculated separately.

We start with the puff strength A, i.e., the integrated Ca^{2+} current during a single puff or, in biophysical terms, a quantity proportional to the amount of Ca^{2+} released per puff. As stated previously, the closing rate is independent of the number of open channels. As we will see, a consequence of this is that the mean puff strength $\langle A \rangle$ is a quadratic function of the number of IP_3Rs in a cluster N as demonstrated in Fig. 2 A_4. In contrast to that, the CV of the puff strength, CV_A, is largely independent of N, see Fig. 2 A_5. Both findings can be understood within our analytical framework presented in the following.

To calculate the mean $\langle A \rangle$, variance $\mathrm{Var}(A)$ and $CV_A^2 = \mathrm{Var}(A)/\langle A \rangle^2$, it is helpful to first determine the *conditional* means $\langle A|n_0 \rangle$ and variances $\mathrm{Var}(A|n_0)$, given a certain number of responding channels n_0, and subsequently to use the law of total mean and variance (58) to relate both to each other:

$$\langle A \rangle = \langle \langle A|n_0 \rangle_A \rangle_{n_0}, \tag{10a}$$

$$\mathrm{Var}(A) = \langle \mathrm{Var}(A|n_0)_A \rangle_{n_0} + \mathrm{Var}(\langle A|n_0 \rangle_A)_{n_0}. \tag{10b}$$

Here, we have explicitly emphasized over which quantity the average was formed but, in the following, will omit the indices for the ease of notation. We can consider the conditional puff strength $(A|n_0)$ to be the sum of n_0 random numbers, namely the area under each "step" of the puff denoted by $(a|n)$:

$$(A|n_0) = \sum_{n=1}^{n_0} (a|n). \tag{11}$$

For instance, for the first puff shown in Fig. 2 A_1 the number of responding channels is $n_0 = 4$ and the area under the puff A_i can be consider to be the sum of four independent random numbers. For the nth step the area $(a|n) = n\tau_n$ is the product of the (stochastic) dwell time τ_n and the (deterministic) number of open channels n. Because τ_n is exponentially distributed, so is $(a|n)$ with a rescaled rate $\lambda_n = \lambda_{cls}/n$.

Since we deal with independent random variables their means and variances sum up and we find:

$$\begin{aligned} \langle A|n_0 \rangle &= \sum_{n=1}^{n_0} \langle a|n \rangle = \sum_{n=1}^{n_0} \frac{n}{\lambda_{cls}} \\ &= \frac{1}{2\lambda_{cls}} n_0(n_0+1), \end{aligned} \tag{12a}$$

$$\begin{aligned} \mathrm{Var}(A|n_0) &= \sum_{n=1}^{n_0} \mathrm{Var}(a|n) = \sum_{n=1}^{n_0} \frac{n^2}{\lambda_{cls}^2} \\ &= \frac{1}{6\lambda_{cls}^2} n_0(n_0+1)(2n_0+1). \end{aligned} \tag{12b}$$

The unconditional mean is readily obtained using Eqs. 10a and 12a as well as the fact that n_0 is uniformly distributed over N:

$$\begin{aligned} \langle A \rangle &= \langle \langle A|n_0 \rangle \rangle = \frac{1}{N} \sum_{n_0=1}^{N} \frac{1}{2\lambda_{cls}} n_0(n_0+1) \\ &= \frac{1}{6\lambda_{cls}} (N+1)(N+2). \end{aligned} \tag{13}$$

It can be seen that the average puff strength is indeed a quadratic function of the number of channels N as pointed out above. The total variance can be calculated according to Eq. 10b using the conditional mean and variance in Eqs. 12a and 12b:

$$\langle \mathrm{Var}(A|n_0) \rangle = \frac{1}{12\lambda_{cls}^2} (N+1)^2(N+2), \tag{14a}$$

$$\mathrm{Var}(\langle A|n_0\rangle) = \frac{1}{60\lambda_{\mathrm{cls}}^2}(N+1)(N+2)\left(3N^2+6N+1\right) - \frac{1}{36\lambda_{\mathrm{cls}}^2}(N+1)^2(N+2)^2. \tag{14b}$$

and adding the two together. This yields an expression that is cumbersome at first glance. However, it turns out that the CV:

$$CV_A^2 = \frac{\langle \mathrm{Var}(A|n_0)\rangle + \mathrm{Var}(\langle A|n_0\rangle)}{\langle A\rangle^2} = \frac{4N^2+18N+8}{5N^2+15N+10}, \tag{15}$$

is a monotonically decreasing function for $N \in \mathbb{N}_{>0}$, bound between 1 and 0.8 as shown in Fig. 2 A_5. The upper bound corresponds to a single channel ($N = 1$) where the puff is made of a single step with puff strength drawn from an exponential distribution, accordingly $CV_A^2 = 1$. In this case only the first term on the r.h.s. of Eq. 10b contributes to the total variance, because there is no variability in the number of responding channels. The lower bound is obtained for infinite cluster sizes $N \to \infty$: In this case the second term on the r.h.s. of Eq. 10b determines the total variance and we obtain

$$\lim_{N\to\infty} CV_A^2 = \lim_{N\to\infty} \frac{\mathrm{Var}(\langle A|n_0\rangle)}{\langle A\rangle^2} = \frac{4}{5}. \tag{16}$$

Hence, even for large clusters consisting of many IP_3R channels the variability of the number of responding channels ensures the strong variability of the puff strength. Fig. 2 A_5 shows the contributions of $\langle \mathrm{Var}(A|n_0)\rangle/\langle A\rangle^2$ (*dotted line*) and $\mathrm{Var}(\langle A|n_0\rangle)/\langle A\rangle^2$ (*dashed line*) to the total (*squared*) CV as a function of the cluster size.

We now turn to the IPI I, that is the time between two subsequent puffs (excluding the duration of the puff itself), see Fig. 2 B_1. In contrast to the puff strength, the IPI statistics depends heavily on the chosen Ca^{2+} concentration c_i; below we numerically illustrate our results for the resting and threshold Ca^{2+} concentrations.

The mean and variance of the IPI are readily obtained if the IPI is considered to be the sum of the exponentially distributed dwell times:

$$I = \sum_{m=1}^{M} \tau_{0_m} \tag{17}$$

where τ_{0_m} are independent random times spend in the states $\omega = 0_m$. It follows that:

$$\langle I\rangle = \sum_{m=1}^{M} \langle \tau_{0_m}\rangle = \frac{M-1}{\lambda_{\mathrm{ref}}} + \frac{1}{\lambda_{\mathrm{opn}}}, \tag{18a}$$

$$\mathrm{Var}(I) = \sum_{m=1}^{M} \mathrm{Var}(\tau_{0_m}) = \frac{M-1}{\lambda_{\mathrm{ref}}^2} + \frac{1}{\lambda_{\mathrm{opn}}^2}, \tag{18b}$$

$$CV_I^2 = \mathrm{Var}(I)/\langle I\rangle^2 = \frac{1+(M-1)\left(\lambda_{\mathrm{opn}}/\lambda_{\mathrm{ref}}\right)^2}{\left(1+(M-1)\lambda_{\mathrm{opn}}/\lambda_{\mathrm{ref}}\right)^2} = 1-(M-1)\frac{2\lambda_{\mathrm{ref}}/\lambda_{\mathrm{opn}}+M-2}{\left(\lambda_{\mathrm{ref}}/\lambda_{\mathrm{opn}}+M-1\right)^2}. \tag{18c}$$

We first discuss the obvious dependence on the number of closed states M. Trivially, the mean IPI increases with M because the system has to traverse more states. In contrast, the variability decreases monotonically with the number of closed states, starting with a $CV_I = 1$ for $M = 1$ (corresponding to a Poisson process) and vanishes for large as $CV_I \propto 1/\sqrt{M}$.

Another interesting question is how the statistics of the IPI depends on the cluster size N which affects the moments only through the opening rate $\lambda_{\mathrm{opn}} \propto N$, see Eq. 7. The inverse mean $\langle I\rangle^{-1}$ is shown in Fig. 2 B_4 and displays a close to linear shape when the Ca^{2+} concentration is at rest $c_i = c_0$ (*solid line* in Fig. 2 B_4). This is reasonable given that in the considered parameter regime in Eq. 18a the first term (independent of N) is much smaller than the second term (proportional to $1/N$), hence the inverse mean IPI is approximately proportional to N. For higher Ca^{2+} concentrations, for instance, at the threshold $c_i = c_T$, the rate λ_{opn} is larger and the dependence of $\langle I\rangle$ on N is more nonlinear (*dashed line* in Fig. 2 B_4).

The irregularity of the IPI is quantified by the CV_I and also depends on the cluster size through λ_{opn}. Specifically, for small clusters the IPI is mainly determined by the dwell time in the state $\omega = 0_1$ and, consequently, almost exponentially distributed with a CV_I close to one. For larger clusters, however, the state $\omega = 0_1$ is left quickly, and the IPI is primarily determined by the concatenation of the refractory states which yields more regular intervals. However, at the resting Ca^{2+} concentration, there is little variation of the CV_I over a moderate range of cluster sizes N because the mean dwell time $\tau_{0_1} = 1/\lambda_{\mathrm{opn}}$ still dominates the IPI for all N (*solid line* in Fig. 2 B_5). A tendency toward lower values of the CV_I can indeed be observed for higher Ca^{2+} concentrations close to the threshold of Ca^{2+} spiking (*dashed line* in Fig. 2 B_5). For much larger opening rates λ_{opn}, encountered at large cluster sizes, the CV_I saturates at $CV_I = 1/\sqrt{M-1}$ for $M > 1$.

The full IPI probability density function $p_{\mathrm{IPI}}(t)$ is obtained as a convolution of $M-1$ exponential densities with a rate λ_{ref} and one exponential density with rate λ_{opn}; this is so because the IPI is the sum of the statistically independent dwell times in the closed states. The result of the convolution integral can be expressed by the lower incomplete gamma function $\gamma(a, t) = \int_0^t dt' \quad t'^{a-1}e^{-t'}$:

$$\begin{aligned} p_{\mathrm{IPI}}(t) &= \lambda_{\mathrm{opn}} p_{0_1}(t) \\ &= \lambda_{\mathrm{opn}} \left(\frac{\lambda_{\mathrm{ref}}}{\lambda_{\mathrm{ref}} - \lambda_{\mathrm{opn}}} \right)^{M-1} \\ &\quad \times \frac{\gamma\left(M-1, \left(\lambda_{\mathrm{ref}} - \lambda_{\mathrm{opn}}\right)t\right)}{(M-2)!} e^{-\lambda_{\mathrm{opn}} t}, \end{aligned} \tag{19}$$

a simple result confirmed for two different Ca^{2+} concentrations in Fig. 2, B_2 and B_3.

Most importantly, for the Langevin approximation derived below, we can calculate the mean μ_x and noise intensity D_x of a single cluster $x(t)$ by means of algebraic equations. One ingredient needed in following is the stationary probability vector of the states, determined by the stationary master equation and the normalization condition:

$$\mathbf{0} = W \cdot \boldsymbol{p}_0, \text{and} \sum_{i \in \Omega} p_0(i) = 1, \tag{20}$$

where $\mathbf{0}$ is the zero vector. The solution of Eq. 20 reads for our specific model:

$$p_0(i) = \begin{cases} \dfrac{N+1-i}{N} \dfrac{1}{\tau_{\mathrm{tot}} \lambda_{\mathrm{cls}}}, & \text{if } i \in [N, \ldots, 1] \\ \dfrac{1}{\tau_{\mathrm{tot}} \lambda_{\mathrm{ref}}}, & \text{if } i \in [0_M, \ldots, 0_2] \\ \dfrac{1}{\tau_{\mathrm{tot}} \lambda_{\mathrm{opn}}}, & \text{if } i = 0_1 \end{cases} \tag{21}$$

This allows to calculate the mean of the puff current:

$$\begin{aligned} \mu_x &= \sum_{i \in \Omega} x(i) \cdot p_0(i) \\ &= \frac{1}{6\lambda_{\mathrm{cls}}} \frac{(N+1)(N+2)}{\dfrac{1}{\lambda_{\mathrm{opn}}} + \dfrac{M-1}{\lambda_{\mathrm{ref}}} + \dfrac{N+1}{2\lambda_{\mathrm{cls}}}} = \frac{\langle A \rangle}{\tau_{\mathrm{tot}}}. \end{aligned} \tag{22}$$

While the determination of the stationary probabilities and the mean follows standard procedures (59,60), the calculation of the noise intensity for the process $x(t)$ is more advanced.

First of all, the noise intensity is defined by

$$D_x = \int_0^\infty d\tau \, C_{xx}(\tau). \tag{23}$$

From this equation it is not so obvious to see that the noise intensity is determined by an algebraic equation. After all the correlation function, $C_{xx}(\tau) = \langle x(t)x(t+\tau) \rangle - \langle x \rangle^2$, requires the time-dependent solution $\boldsymbol{p}(t)$ of the master equation. However, we can use the fact that we only need the integral of the correlation function to avoid solving the time-dependent problem; a similar trick has been applied to calculate the correlation time (61) and the diffusion coefficient (62,63) of systems described by a FPE. To that end we express the correlation function in terms of transition and stationary probabilities:

$$\begin{aligned} D_x &= \int_0^\infty d\tau \, C_{xx}(\tau) \\ &= \int_0^\infty d\tau \, \langle x(t+\tau)x(t) \rangle - \langle x \rangle^2 \\ &= \int_0^\infty d\tau \sum_{i,j} [x(i)x(j)p(i, t+\tau | j, t)p_0(j) \\ &\qquad - x(i)x(j)p_0(i)p_0(j)] \\ &= \sum_{i,j} x(i)x(j) \int_0^\infty d\tau \; [p(i, t+\tau | j, t) - p_0(i)]p_0(j) \\ &= \sum_{i,j} x(i)x(j) f(i,j) p_0(j). \end{aligned} \tag{24}$$

Note that the sums run again over all possible states of a cluster. Formally, we still have to find the time-dependent transition probabilities $p(i, t' | j, t)$, however, it turns out that the auxiliary function $f(i,j)$, that contains integrals of probability functions, is much simpler to calculate. In particular, the functions $f(i,j)$ can be determined as the solution of an algebraic instead of a differential equation which simplifies the evaluation considerably. To make this clear consider the lth row of the master equation Eq. 4 with the additional condition that the state at time t is known, i.e., $p(l,t) = \delta_{l,j}$:

$$\begin{aligned} \dot{p}(l, t+\tau | j, t) &= \sum_i w_{l,i} p(i, t+\tau | j, t) \\ \int_0^\infty d\tau \; \dot{p}(l, t+\tau | j, t) &= \int_0^\infty d\tau \sum_i w_{l,i} [p(i, t+\tau | j, t) - p_0(i)] \\ p_0(l) - \delta_{l,j} &= \sum_i w_{l,i} f(i,j) \end{aligned} \tag{25}$$

to get from the first to the second line we have subtracted the stationary probability $0 = \dot{p}_0(l) = \sum_i w_{l,i} p_0(i)$ on the r.h.s. and integrated both sides. This yields a set of algebraic equations:

$$\boldsymbol{p}_0 - \boldsymbol{e}_j = W \cdot \boldsymbol{f}_j \tag{26}$$

with $\boldsymbol{f}_j = (f(1,j), f(2,j), \cdots)^T$ and $\boldsymbol{e}_j$ is the unit vector in the jth direction. As in the case of the stationary probability, Eq. 26 alone does not determine $\boldsymbol{f}_j$ unambiguously but requires an additional condition that can be found by the following consideration:

$$\begin{aligned} \sum_i f(i,j) &= \int_0^\infty d\tau \sum_i [p(i, t+\tau | j, t) - p_0(i)] \\ &= \int_0^\infty d\tau \, [1 - 1] = 0. \end{aligned} \tag{27}$$

In conclusion, we can determine the auxiliary functions $f(i,j)$ using Eq. 26 and the additional condition Eq. 27.

Together with the stationary probabilities these determine the noise intensity by:

$$D_x = \sum_i \sum_j x(i)x(j)f(i,j)p_0(j). \tag{28}$$

Reduction of the two-component model to a stochastic IF model: Diffusion approximation of the puff current

An essential property of Ca^{2+} signaling is its hierarchical organization into blips, puffs, and spikes. In the previous section, we looked at puff statistics determined by the kinetic model of an IP_3R cluster. These puffs give rise to a stochastic Ca^{2+} current, the puff current, that feeds into the dynamics of the cytosolic Ca^{2+} concentration and influences associated statistics, for instance, statistics of the ISIs $T_i = t_{i+1} - t_i$ that is the time between two subsequent Ca^{2+} spikes. Calculating ISI statistics from Eq. 2 is difficult because the noise originating from the puff current is a complicated stochastic process, i.e., it does not correspond in general to the simple white Gaussian noise that permits an analytical treatment via the FPE. However, the timescale separation between the puff current and c_i leak current allows for a diffusion approximation in which the stochastic puff current j_{puff} is substituted by a deterministic mean and Gaussian white noise. The resulting Langevin equation can be efficiently numerically integrated and key statistics of c_i and the ISI can be calculated analytically by means of the associated FPE. Discrete-time Markov chains have already been approximated by Langevin equations in the past. To this end, it is usually assumed that the fraction of channels (or clusters in our case) in each state of the Markov chain can be considered as a continuous random variable (see, for instance, (64)). The disadvantage of this method is that the number of channels/clusters must be large compared with the number of states—a condition that cannot be tested experimentally. In contrast, our method relies solely on the observed timescale separation.

To derive the approximate Langevin equation, we first consider Eq. 2 integrated over a short time bin (time window):

$$\begin{aligned} c_i(t+\Delta t) &= c_i(t) - \int_t^{t+\Delta t} dt'(c_i(t') - c_0)/\tau \\ &\quad + \int_t^{t+\Delta t} dt'\, p\Delta c_{er} \sum_{k=1}^{K} x_k(t') \end{aligned} \tag{29}$$

and define:

$$Y(t;\Delta t) = \frac{1}{\Delta t}\int_t^{t+\Delta t} dt' \sum_{k=1}^{K} x_k(t'). \tag{30}$$

Here, $Y(t;\Delta t)$ can be regarded as a box-filtered version or moving average of the cluster activity $\sum_k x_k(t)$ and we have explicitly highlighted its parametric dependence on the integration window Δt. As a result of the filtering, $Y(t;\Delta t)$ is continuous random process with piecewise continuous derivative. The goal is to find a time bin Δt so that the following two conditions are met. First, Δt must be chosen *large enough* for $\sum_k x_k$ to experience many transitions. This will ensure that, according to the central limit theorem, $Y(t;\Delta t)$ is Gaussian distributed with mean μ_Y and variance σ_Y^2 (calculate in the appendix).

Secondly, Δt has to be chosen *small enough* so that $c_i(t)$ does not change considerably over this time bin. If these two constraint can be met simultaneously, Eq. 29 can be approximated by:

$$\begin{aligned} c_i(t+\Delta t) &\approx c_i(t) - (c_i(t) - c_0)\Delta t/\tau + p\Delta c_{er} Y(t;\Delta t)\Delta t, \\ &= c_i(t) - (c_i(t) - c_0)\Delta t/\tau + p\Delta c_{er}\mu_Y \Delta t \\ &\quad + p\Delta c_{er}\sigma_Y(\Delta t)\nu(t)\Delta t, \end{aligned} \tag{31}$$

with the zero mean and unit variance Gaussian random numbers $\nu(t)$.

Note that the mean $\mu_Y(c_i)$ and more importantly the variance $\sigma_Y^2(c_i)$ are c_i dependent due to the c_i dependence of the opening rate. Eq. 31 has strong similarities to an Euler integration scheme of a Langevin equation. An important difference is that the Gaussian random numbers $\nu(t)$ in Eq. 31 are not uncorrelated, corresponding to a nonvanishing correlation time τ_Y of the process $Y(t;\Delta t)$; the correlation time is shown in Fig. 4 *D*. If, however, this correlation time is short compared with the timescale of the c_i leak current, we may assume the Gaussian random numbers to be uncorrelated. In the same limit one can show (see appendix) that the standard deviation $\sigma_Y(\Delta t) \propto 1/\sqrt{\Delta t}$, resulting in the correct scaling of the noise term in the discretized Langevin equation (65) and we obtain for the puff current

$$j_{puff} \approx \mu_{puff}(c_i) + \sqrt{2D_{puff}(c_i)}\xi(t), \tag{32}$$

so that Eq. 31 approximately corresponds to

$$\dot{c}_i = -(c_i - c_0)/\tau + \mu_{puff}(c_i) + \sqrt{2D_{puff}(c_i)}\xi(t),$$

$$\text{if } c_i(t) = c_T \to t_i = t \text{ and } c_i(t) = c_R. \tag{33}$$

Here, $\mu_{puff} = p\Delta c_{er}\mu_Y$ is the mean puff current, $\xi(t)$ is a zero mean Gaussian white noise with $\langle \xi(t)\xi(t')\rangle = \delta(t - t')$, and $D_{puff} = (p\Delta c_{er})^2\sigma_Y^2(\Delta t)\Delta t/2$ is the noise intensity. To summarize, we have first approximated the discontinuous cluster activity $\sum_k x_k(t)$ by a coarse-grained continuous random process $Y(t)$ that is assumed to be Gaussian distributed. In a second step this random process is approximated by a Gaussian white noise, hence assumed to be uncorrelated on the relevant timescale of the c_i dynamics. The resulting

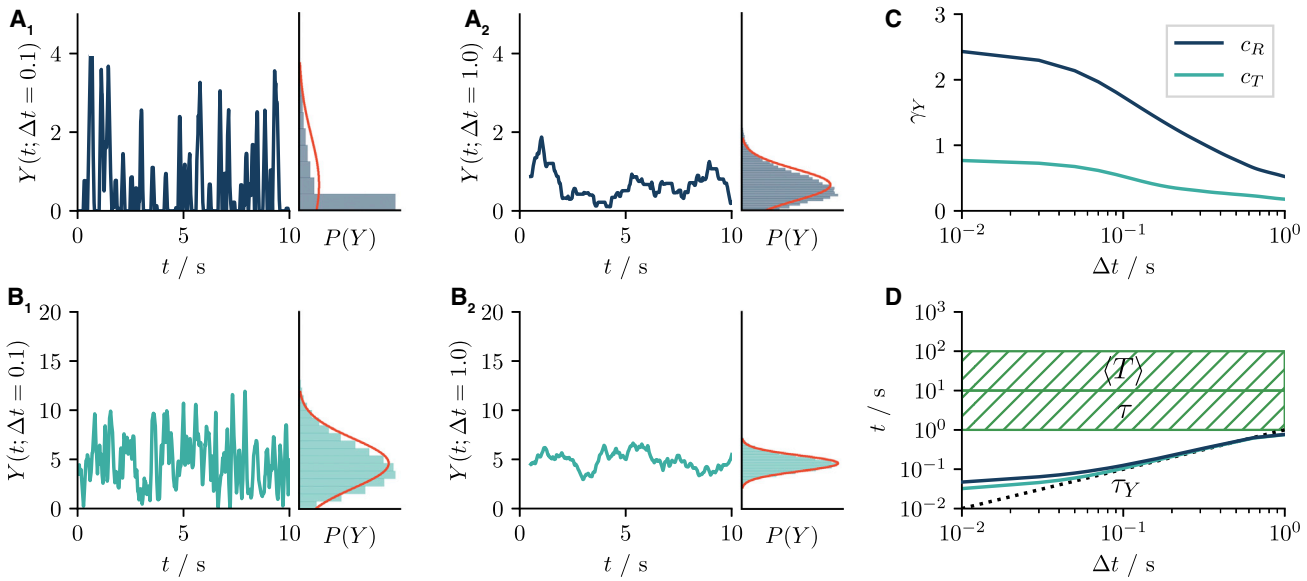

FIGURE 4 Diffusion approximation of the puff current. For the puff current to be well approximated by a Gaussian white noise, there has to be a time bin Δt, so that $Y(t;\Delta t)$ is 1) Gaussian distributed and 2) shortly correlated compared with every other timescale present in the system. (*A* and *B*) Show exemplary time series of the random process $Y(t;\Delta t)$ together with the probability distribution $P(Y)$ (*histogram*) for two different values of the Ca^{2+} concentration c_i ($c_i = c_R$ in (*A*) and $c_i = c_T$ in (*B*). We also show the effect of different time bins Δt over which the cluster activity $\sum x_k$ was averaged according to Eq. 30: $\Delta t = 0.1$ (A_1, B_1) and $\Delta t = (A_2, B_2)$. The probability distribution $P(Y)$ resembles more strongly the desired Gaussian distribution (*solid red line*) when Δt and c_i are larger because then a larger number of transitions in the considered time bin occur. In (*C*), the deviation of $P(Y)$ from a Gaussian distribution is quantified by the skewness $\gamma_Y = \langle(Y - \langle Y\rangle)^3\rangle / \langle(Y - \langle Y\rangle)^2\rangle^{3/2}$ of $P(Y)$, which decreases with increasing Δt. (*D*) Illustrates the timescale separation between the mean ISI $\langle T\rangle$, the timescale of the c_i leak current τ, and the correlation time τ_Y of the random process $Y(t)$. The latter approaches $\tau_Y = \Delta t$ for large values of Δt (*dotted line*). Parameters are chosen according to Fig. 2 and $K = 10$. To see this figure in color, go online.

stochastic differential equation with a c_i-dependent noise intensity is an equation with multiplicative noise. Such an equation requires an interpretation (66) the most popular of which are the ones by Ito, by Stratonovich, and by Klimontovich and Hänggi (67), and it is not immediately clear which one of them, if any, should be used for our model. However, it is known that according to Wong and Zakai (68), a Langevin equation should be interpreted in the Stratonovich sense if the multiplicative noise is an approximation of a continuous random process that has a piecewise continuous derivative, as it is the case for $Y(t)$. The corresponding FPE for the Stratonovich-interpreted Eq. 33 is given by:

$$\partial_t p(c_i,t) = \partial_{c_i}\Big[(c_i - c_0)/\tau - \mu_{\text{puff}}(c_i) - D'_{\text{puff}}(c_i)/2 + \partial_{c_i} D_{\text{puff}}(c_i)\Big]p(c_i,t) + r_0\delta(c_i - c_R). \tag{34}$$

where $D'_{\text{puff}}(c_i)/2$ is the Stratonovich drift and the prime denotes the derivative with respect to c_i. The unusual source term $r_0\delta(c_i - c_R)$ accounts for the influx of probability due to the reset of the trajectories that reach the threshold (for the analytical treatment, see the literature from computational neuroscience (32,69–71)). Eq. 34 is completed by the natural boundary condition $\lim_{c_i\to-\infty} p(c_i,t) = 0$, the absorbing boundary condition at the threshold $p(c_T,t) = 0$, and the normalization condition $\int dc_i\, p(c_i,t) = 1$. Even though we opted above for the Stratonovich interpretation, it is nevertheless interesting to explore the consequence of the interpretation for the ISI statistics which is done below (see Fig. 6 and surrounding discussion). In brief, the choice of the interpretation has only a minor effect on the ISI statistics in the biophysically relevant parameter range.

Regarding the spike train produced by the IF model Eq. 33, we note that irrespective of the specific form of the Ca^{2+}-dependent drift and noise terms, the model always generates a renewal process (72), i.e., a point process with statistically independent intervals between adjacent spikes. This is so because the reset of the Ca^{2+} variable c_i to a fixed value c_R at the end of one interval erases any memory about this interval and the uncorrelated noise process $\xi(t)$, by definition, cannot carry any memory from one ISI to the next either.

Statistics of the subthreshold cytosolic Ca^{2+} and the spike train

In the previous section we have introduced a one-dimensional Langevin approximation of the two-component model and stated the associated FPE. In particular the latter equation permits the analytical calculation of statistics of interest of the subthreshold Ca^{2+} concentration and of the ISIs (see appendix). Here, we compare these analytical results to numerical simulations of the two-component model Eq. 2. We will also give an overview how the spike statistics

depends on the system parameters, specifically the timescale of the leak current τ, the permeability-like parameter p, and the number of clusters K, i.e., the parameters that are presumably most prone to cell-to-cell variability.

By means of the Langevin approximation of the two-component model two firing regimes can be distinguished. In the mean-driven regime the model crosses the spiking threshold even in the absence of fluctuations and spiking is typically more regular. In the excitable (fluctuation-driven) regime, on the contrary, the threshold is crossed only due to noise and spiking is more variable. The two regimes can be distinguished by the deterministic drift term in the Langevin equation, $f(c_i) = -(c_i - c_0)/\tau + \mu_{puff}(c_i)$, which in the mean-driven regime is positive for all subthreshold Ca^{2+} concentration, $c_i < c_T$, but has a zero for some $c_i^* < c_T$ in the excitable case. The regimes are separated by the condition that the zero of f is equal to the threshold, $f(c_T) = 0$, which implies $(c_T - c_0)/\tau = \mu_{puff}(c_T)$, The fact that the mean puff current depends linearly on the permeability-like parameter $\mu_{puff}(c_T) = p\Delta c_{er} K \mu_x$ (with μ_x defined in Eq. 22) leads to a simple condition for the critical values of τ and p:

$$\tau p = \frac{c_T - c_0}{\Delta c_{er} K \mu_x}. \tag{35}$$

The behavior of the two-component model in the mean-driven and excitable regime is shown in Fig. 5, *A* and *B*, respectively. In Fig. 5, A_1 and B_1 we show typical time series of the Ca^{2+} concentration and puff current and additionally indicate the corresponding ISI sequences. It can be easily seen that spiking is more regular in the mean-driven regime than in the excitable regime.

In Fig. 5, A_2 and B_2 the corresponding stationary probability densities $p_0(c_i)$, obtained from stochastic simulation of the two-component model (*histograms*), are compared with the theoretical predictions (*red line*) according to Eq. 61 and demonstrate excellent agreement. In the mean-driven regime the probability is close to uniform (Fig. 5 A_2) due to the little variation shown by the drift (cf. *inset* Fig. 5 A_2). In the excitable regime the deterministic drift has a zero, see inset Fig. 5 B_2. The system spends more time around the zero, which is reflected in a pronounced maximum of the probability density (Fig. 5 B_2). The maximum is not exactly at the zero but at a somewhat smaller concentration due to the interplay between the multiplicative noise and the nonlinear drift term.

In Fig. 5, A_3 and B_3 we show the resulting ISI density obtained from simulations of the two-component model by histograms. In the mean-driven regime the distribution of the ISIs is strongly peaked (Fig. 5 A_3): the sequence of ISIs is rather regular with a moderate CV of $CV_T = \sqrt{\langle \Delta T^2 \rangle}/\langle T \rangle = 0.2$. The probability density of the ISI is well described by both an inverse Gaussian and gamma distribution:

$$p_{IG}(T) = \sqrt{\frac{\langle T \rangle}{2\pi CV_T^2 T^3}} \exp\left(-\frac{(T - \langle T \rangle)^2}{2\langle T \rangle CV_T^2 T} \right), \tag{36}$$

$$p_{Gamma}(T) = \frac{1}{\Gamma\left(1/CV_T^2\right) T} \left(\frac{T}{\langle T \rangle CV_T^2} \right)^{1/CV_T^2} \exp\left(-\frac{T}{\langle T \rangle CV_T^2} \right) \tag{37}$$

where $\Gamma(a) = \int_0^\infty dt' t'^{a-1} e^{-t'}$ is the gamma function. This densities are fully determined by the mean and CV of the ISI. We use two versions of the formulas: one where we determine $\langle T \rangle$ and CV_T from stochastic simulations of the two-component model (*dashed line*) and another one where we calculate $\langle T \rangle$ and CV_T analytically using Eq. 62 and Eq. 68 from the Langevin approximation. It turns out that in the mean-driven regime both densities and versions agree very well, the latter indicates that the Langevin equation provides a good approximation.

In the excitable case, the ISI sequence is much more variable with a $CV_T = 0.8$ and its probability density (Fig. 5 B_3) displays a pronounced skewness. Surprisingly, even in this case the inverse Gaussian Eq. 36 provides a good description when we use the mean and CV obtained from simulation of the two-component model, whereas the mean and CV calculated from Eq. 62 and Eq. 68 leads to a somewhat more peaked distribution. Here, the Langevin approximation does not work so well anymore because in the excitable regime the timescales of the leak and the puff currents are no longer strongly separated.

Going beyond the two specific sets of parameters inspected so far, we show in Fig. 6, *A* and *B* the mean and CV of the ISIs obtained from stochastic simulations of the two-component model at values of the timescale τ and permeability-like parameter p varied over two orders of magnitude. Plausibly, the mean ISI (Fig. 6 *A*) drops systematically with growing p (which increases the mean and noise intensity of the puff current) and growing τ (which decreases the leak current). We also show the boundary between excitable and mean-driven regimes according to Eq. 35 (*dashed red line*). Because we consider only noise originating from the IP_3R clusters as the sole source of fluctuations, there is also a large chunk of the parameter space at small values of p and τ where no spiking is observed (*white area*) and the excitable regime attains only a small portion below the bifurcation line. The CV (Fig. 6 *B*) displays a more complicated dependence on the parameters. It is usually high, close to one, in the excitable regime (73) and drops drastically as soon as we cross the bifurcation line by increasing p or τ. In the limit of large τ, i.e., when the leak current becomes negligible, the CV saturates. In contrast, for large p the CV keeps increasing. This is presumably due to the increasing noise intensity combined

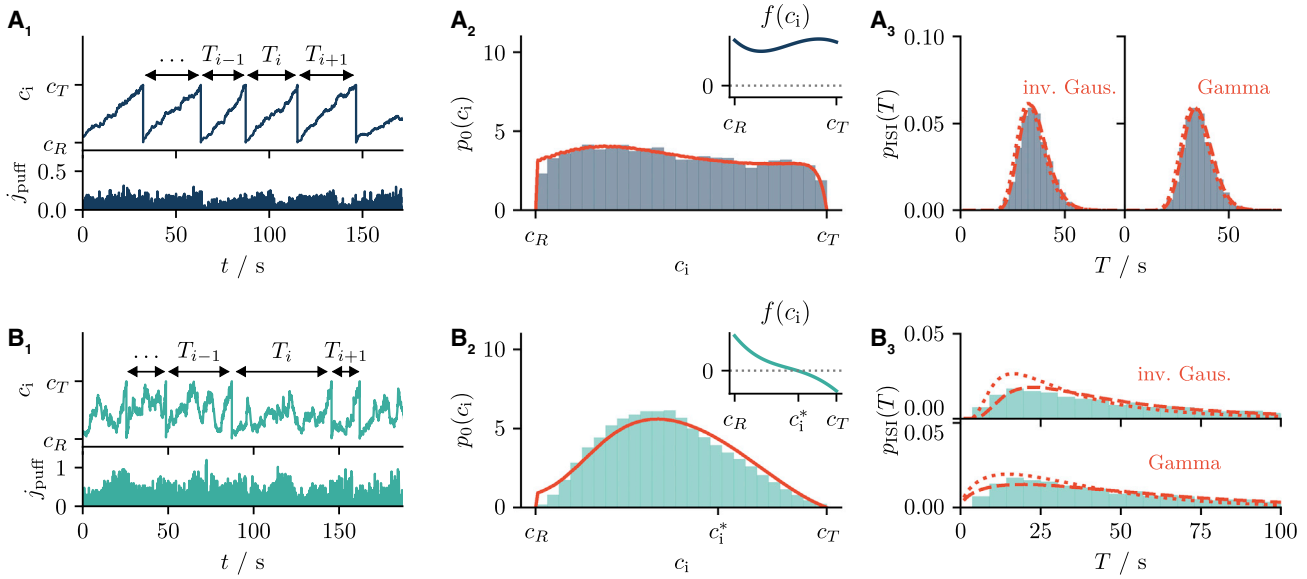

FIGURE 5 Two-component model in the mean-driven and excitable regime. (*A* and *B*) The model is in the mean-driven and excitable regime, respectively. (A_1 and B_1) Show the subthreshold dynamics of c_i and the puff current j_{puff}. Already with the naked eye it can be seen that the corresponding ISI sequence marked by black arrows is more regular in (A_1) than in (B_2). (A_2 and B_2) We compare the corresponding subthreshold probability densities $p_0(c_i)$ obtained from stochastic simulations of the two-component model (*histograms*) to the theoretical prediction according to Eq. 61 (*red lines*). The insets in (A_2) and (B_2) shows the drift $f(c_i)$ that is always positive in the mean-driven regime (A_2) but exhibits a zero at c_i^* in the excitable regime (B_2). (A_3 and B_3) The ISI densities determined from numerical simulations (*histograms*) are compared with inverse Gaussian and gamma distributions (*red lines*) as indicated by the red text. Both distributions are uniquely determined by the mean $\langle T\rangle$ and CV CV_T that have been taken either directly from stochastic simulations of the two-component model (*dashed red lines*) or calculated according to Eq. 62 and Eq. 69 (*dotted red lines*). In the mean-driven regime all four variants are in excellent agreement with the ISI density obtained from the two-component model. In the excitable regime the inverse Gaussian provides a better estimate than the gamma distribution to the ISI density obtained from stochastic simulations of the two-component model. In addition, mean and CV obtained from the two-component model and the Langevin approximation begin to differ so that the distributions (*dashed* and *dotted red lines*) disagree. Parameters: $K = 10$, (A): $\tau = 5, p = 1.5\times10^{-2}$, ($B$): $\tau = 1, p = 6\times10^{-2}$. To see this figure in color, go online.

with the fact that the leak current becomes less important for $p\to\infty$.

We can repeat the same simulations using the Langevin Eq. 33 to obtain the mean and CV, and we can do this not only for the Stratonovich interpretation of this equation, on which our analytical calculations are based, but also for the other two popular interpretations. In Fig. 6, C_1–C_3 and D_1–D_3 we show the relative differences between mean and CV obtained from stochastic simulation of the two-component model and the Langevin equation in the three interpretations as discussed around Eq. 34. We find that in the biophysically relevant parameter range the three interpretations yield similar results and thus the interpretation of the stochastic differential equation is not a vital issue for our model.

Returning to the two specific sets of parameters, in Fig. 7 we show essential ISI statistics of the model. In Fig. 7, A_1 and B_1 we plot the firing rate $r_0 = 1/\langle T\rangle$ as a function of the stimulus amplitude, the relative IP_3 concentration s (the *arrow* indicates the value of s that was used so far and is used in the remaining panels of this figure). Each circle corresponds to a stochastic simulation of the two-component model and is color-coded according to the corresponding CV_T obtained from the same simulation. The theoretical prediction of the firing rate according to Eq. 62 shows excellent agreement with the simulation results in the mean-driven regime (Fig. 7 A_1) and displays small deviations in the excitable regime (Fig. 7 B_1). We note the similarity of these rate-versus-stimulus curves to the f-I curves (frequency versus input current) used in computational neuroscience (see, e.g., (26,74)).

Next we consider the spike *count*, the integral of the spike *train* $z(t) = \sum_i \delta(t - t_i)$:

$$N(t) = \int_0^t dt'\, z(t'), \tag{38}$$

and plot in Fig. 7, A_2 and B_2 an important statistical measure characterizing count variability, namely the Fano factor:

$$F(t) = \frac{\langle \Delta N(t)^2\rangle}{\langle N(t)\rangle}. \tag{39}$$

This measure compares the variance to the mean of the spike count as a function of the counting window t. For time windows t much smaller than the mean ISI, finding a spike in that window is essentially a Poisson process so that $\lim_{t\to0} F(t) = 1$ (75). At intermediate times, the Fano factor decreases linearly (not very apparent due to the used logarithmic scale) up to a characteristic time which is roughly the mean ISI. For large values of t and

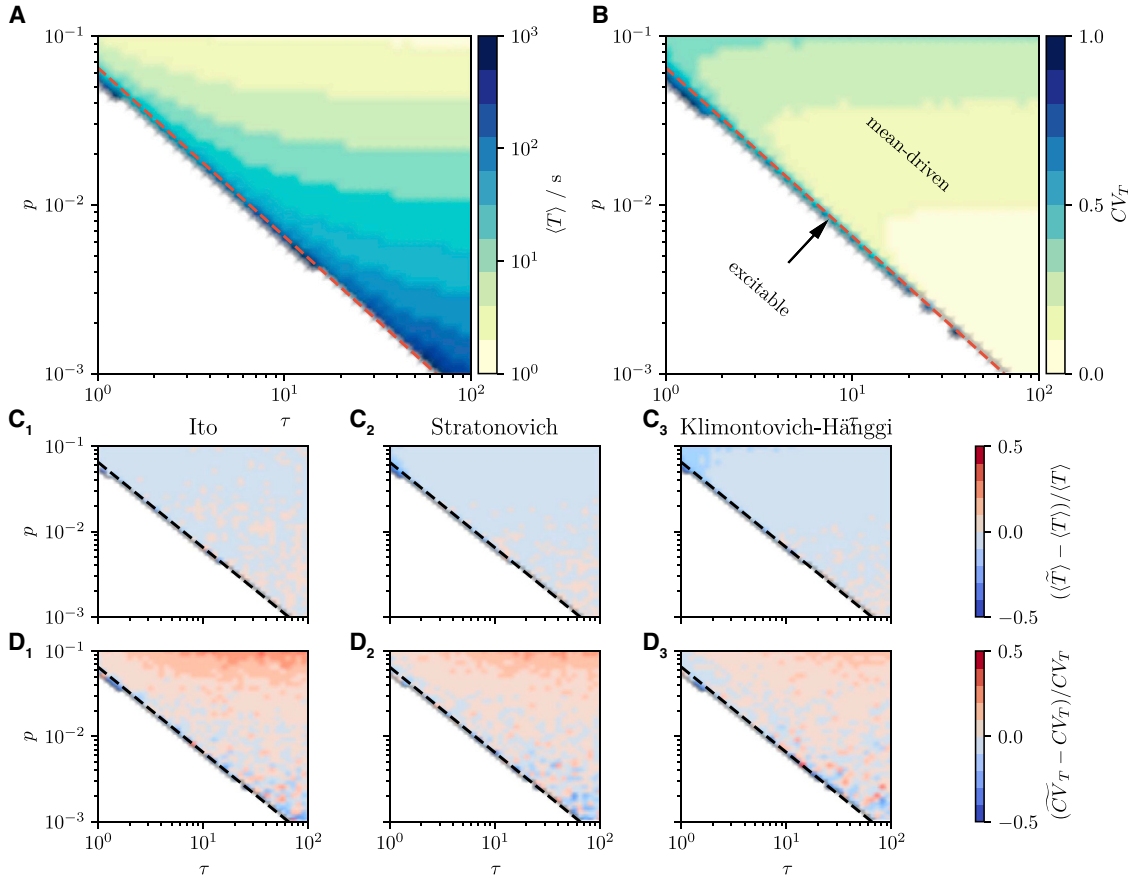

FIGURE 6 Meta statistics of the two-component model and stochastic interpretation of the Langevin equation. (*A* and *B*) Show the mean and CV of the ISI obtained from simulations of the two-component model for a large range of the leak current's time constant τ and permeability-like parameter p. In both panels the red dashed line shows the bifurcation according to Eq. 35. Above the bifurcation line, in the mean-driven regime, the ISIs are typically regular with small CVs and spiking is observed for all parameters. Below the bifurcation line the ISIs are highly irregular with large CV and spiking is observed only for a small range of parameters. In (C_1–C_3) and (D_1–D_3) we compare the mean and CV obtained from simulations of the Langevin approximations ($\langle \tilde{T} \rangle$ and $\widetilde{CV}_T$) in the three most common interpretations to the same statistics obtained from the simulations of the two-component model. Relative deviations are color coded so that blue corresponds to an underestimation and red corresponds to an overestimation of the shown statistics. In any case the relative deviations are small so that the interpretation of the Langevin equation with multiplicative noise is not a major issue here. Parameters: $K = 10$. To see this figure in color, go online.

assuming that the spike train is renewal, as we have argued previously, the Fano factor saturates at the squared CV $\lim_{t\to\infty} F(t) = CV_T^2$ (72), which is confirmed in the figure as well.

Finally, we turn to the power spectrum of the spike train $z(t)$, defined by:

$$S(f) = \lim_{T\to\infty} \frac{\langle |\tilde{z}(f)|^2 \rangle}{T}, \tag{40a}$$

$$\tilde{z}(f) = \int_0^T dt\, z(t) e^{i2\pi ft}, \tag{40b}$$

where is the Fourier transform. In the renewal case the spike train is fully determined by the ISI density and the power spectrum can be related to its Fourier transform $\tilde{p}_{\mathrm{ISI}}(f)$ as follows (76):

$$S_{\mathrm{renew}}(f) = \frac{1}{\langle T \rangle} \frac{1 - |\tilde{p}_{\mathrm{ISI}}(f)|^2}{|1 - \tilde{p}_{\mathrm{ISI}}(f)|^2}, \tag{41a}$$

$$\tilde{p}_{\mathrm{ISI}}(f) = \int_0^\infty dt\, p_{\mathrm{ISI}}(t) e^{i2\pi ft}. \tag{41b}$$

The Fourier transformed of the inverse Gaussian distribution Eq. 36 is given by:

$$\tilde{p}_{\mathrm{IG}}(f) = \exp\left(\frac{1 - \sqrt{1 - 4\pi i f \langle T \rangle CV_T^2}}{CV_T^2} \right) \tag{42}$$

In Fig. 7, A_3 and B_3 we show the power spectrum directly calculate from the spike train of the two-component model according to Eq. 40 (*blue lines*) and compare it to the power spectrum of an inverse Gaussian ISI density according to Eq. 41 and Eq. 42. The more regular spiking in the

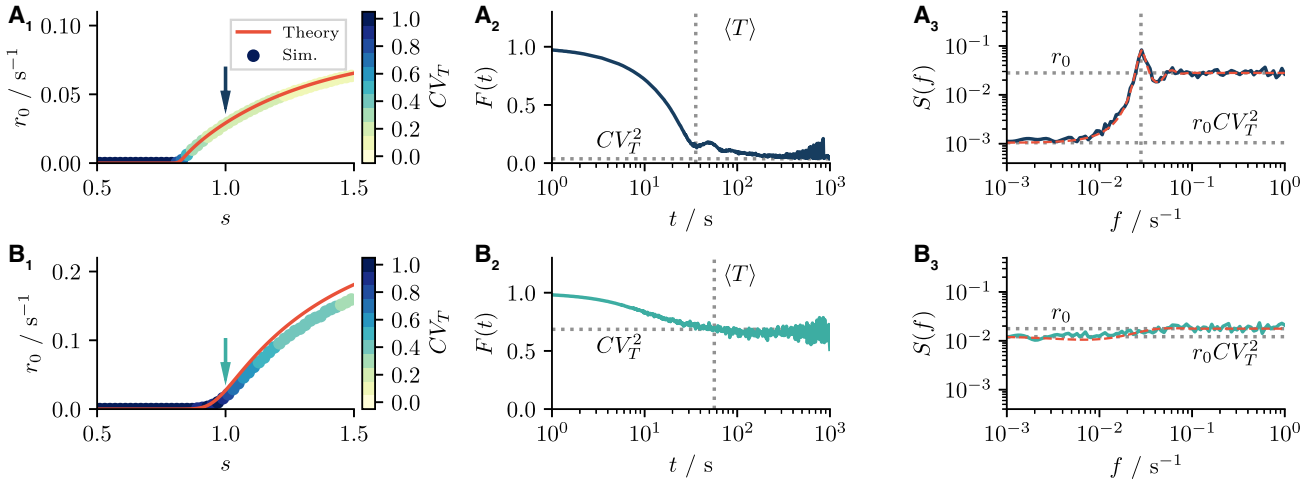

FIGURE 7 Spike-train statistics in the mean-driven and excitable regime. (*A* and *B*) The model is in the mean-driven and excitable regime, respectively. (A_1 and B_1) Show the firing rate $r_0 = 1/\langle T \rangle$ obtained from simulations of the two-component model (*circles*) and theoretical prediction according to Eq. 62 (*red line*) both as a function of the relative IP_3 concentration s. The dots are colored coded according to the CV_T. Arrows indicate the value of s that has been used in the previous figures and is used for the remaining plots. (A_2 and B_2) Show the Fano factor that compares the variance to the mean of the spike count. Horizontal dotted lines indicate the long-time limit $F(t \to \infty) = CV_T^2$ that is approached if the spike train is renewal. Vertical lines indicate the mean ISI $\langle T \rangle$ that defines a characteristic time up to which the Fano factor decreases almost linearly (difficult to see in the lin-log presentation of the plot). (A_3 and B_3) Depict the power spectrum directly computed from the simulated spike train (*blue lines*) and from Eq. 41 using an inverse Gaussian distribution according to Eq. 42 (*dashed red line*). Horizontal lines indicate the low frequency limit of a renewal spike train $S(f = 0) = r_0 CV_T^2$ and high frequency limit $S(f \to \infty) = r_0$. Parameters: $K = 10$, (*A*): $\tau = 5$, $p = 1.5 \times 10^{-2}$, (*B*): $\tau = 1$, $p = 6 \times 10^{-2}$. To see this figure in color, go online.

mean-driven regime becomes apparent by a pronounced peak of the power spectrum at the firing rate $f = r_0$. In the excitable case, the spectrum is rather flat close to the power spectrum of a Poisson process (which would be perfectly flat). In both cases the spike-train power spectrum, as known from point process theory, saturates at the firing rate for $f \to \infty$ and attains the value $r_0 CV_T^2$ for $f \to 0$; these limits are also confirmed in the plot.

Spike train statistics of stimulated HEK cells

Here, we compare ISI statistics measured from HEK cells under constant stimulation, as described in (10,14), to those of an appropriately fitted two-component model. Regarding the experimental data, because long traces of Ca^{2+} signals are notoriously hard to measure, it is difficult to achieve ISI sample sizes that suffice to meaningfully determine the ISI density, Fano factor and power spectrum. To overcome this problem we pursue a similar strategy as suggested by (77) and rescale the time for each spike train. Specifically, we normalize and pool the corresponding ISI sequences, similar to the one shown in Fig. 1 *A*, from 29 different HEK cells as follows. In a first step we select from the available data only the ISI sequences that become stationary according to visual inspection (29/36 sequences). In a second step we perform for the selected sequences a fit of the ISIs T_i by an exponential function, $T_\infty - (T_\infty - T_0)\exp(-i/n_{tr})$, and truncate the sequences by the first $1.5 n_{tr}$ ISIs (rounded up, yielding on average 6 transient out of 20 total intervals). In a third step we normalize the sequences by dividing each interval by the sequence's mean. Finally, we concatenate the normalized sequences to obtain a single long sequence of ISIs that does not distinguish between different cells anymore and from which we calculate the statistics of interest. It should be clear that both the mean of this ISI sequence and the firing rate of the corresponding spike train are equal to one.

To find the parameter set for the two-component model we require that the model's ISI sequence should have the same mean value $\langle T_{\text{exp}} \rangle \approx 160$ s and $CV_{T,\text{exp}} \approx 0.15$ as the experimental data before and after rescaling, respectively. As our model has many parameters, we fix cluster parameters according to the table in Fig. 2 and use $K = 10$. The remaining parameters τ and p are given by the intersection of the contour lines for $\langle T \rangle = \langle T_{\text{exp}} \rangle$ from Fig. 5 *A* and for $CV_T = CV_{T,\text{exp}}$ from Fig. 5 *B*. As illustrated in Fig. 8 *A* (where we also show again the color-coded CV for comparison), there seems to be just one such intersection, hence τ and p are uniquely determined by the given mean and CV (for a related problem, see (78)). Interestingly, the intersection point is very close to the bifurcation line but within the mean-driven regime. Simulated spike trains of the two-component model at the found parameter set ($\tau = 1.44 \times 10^1$, $p = 4.77 \times 10^{-3}$) are then rescaled by the mean ISI to make them comparable to the experimental data.

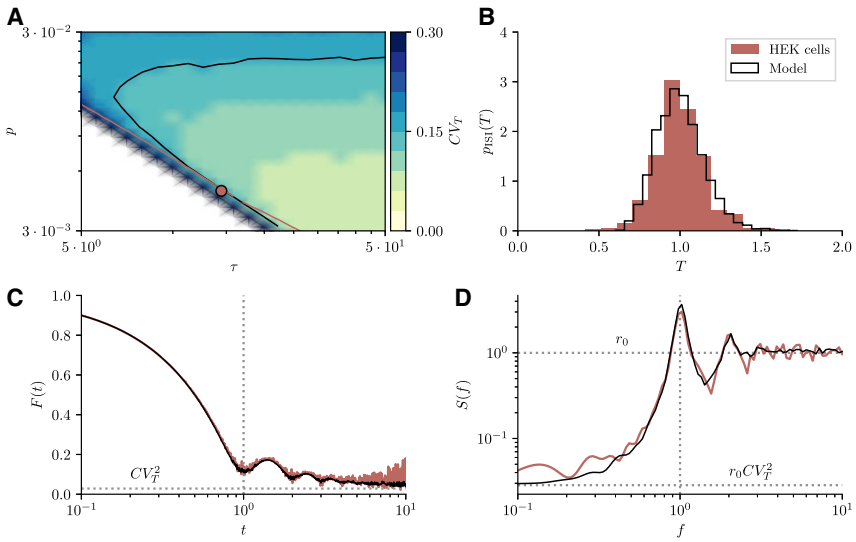

FIGURE 8 Comparison of spike-train statistics from stimulated HEK cells and two-component model. Spike trains from 29 stimulated HEK cells have been rescaled and concatenated as described in the main text to obtain a long sequence with an average ISI $\langle T_{\mathrm{exp}} \rangle \approx 160$ s (before rescaling) and CV $CV_{T,\mathrm{exp}} \approx 0.15$ (after rescaling). (*A*) Shows the contour lines for $\langle T \rangle = \langle T_{\mathrm{exp}} \rangle$ (*black line*) and $CV_T = CV_{T,\mathrm{exp}}$ (*red line*). The intersection of these lines lies in the mean-driven regime close to the bifurcation and uniquely defines the model parameters ($\tau = 1.44 \times 10^1$, $p = 4.77 \times 10^{-3}$) used to generate a simulated spike train that reproduces the experimental mean and CV. (*B*) Compares the rescaled ISI densities obtained from stimulated HEK cells and from the two-component model. (*C*) Displays the corresponding Fano factors $F(t)$ of the associated spike counts. Both factors saturate at CV_T^2 for $t \to \infty$ (*dotted horizontal line*) suggesting that not only the simulated but also the experimental spike train is renewal. (*D*) We compare the power spectra $S(f)$ of the two sequences. The low frequency limit $S(f = 0) = r_0 CV_T^2$ again suggesting that the experimental spike train is renewal. To see this figure in color, go online.

In Fig. 8 *B* the ISI distribution of the rescaled and concatenated spike train obtained from stimulated HEK cells (*red histogram*) is compared with the rescaled ISI distribution obtained from stochastic simulations of the two-component model (*black line*). Given the limited amount and temporal accuracy of the experimental data, the two probability densities agree well with each other. The Fano factors for the experimental (*red line*) and simulated (*black line*) spike trains are show in Fig. 8 *C* and display excellent agreement. In particular, the Fano factor calculated from the experimental data is more similar to the Fano factor of our model in the mean-driven than in the excitable regime (cf. Fig. 7). Finally, in Fig. 8 *D* we present the power spectrum of the experimental spike train (*red line*) and compare it to the spectrum of the model (*black line*). Again, the two spectra show excellent agreement in terms of the low frequency limit, height of the peak at $f = 1/\langle T \rangle$ as well as the high-frequency limit. The latter is not surprising because for $f \to \infty$ the power spectrum always saturates at the firing rate $\lim_{f \to \infty} S(f) = r_0$. The low-frequency limit of the power spectrum is informative because it is related to the firing rate and CV in a simple manner $S(f = 0) = r_0 CV_T^2$ if the spike train is renewal. The fact that the power spectrum indeed saturates at this limit thus indicates that the spike train is renewal and that the ISIs are uncorrelated. This is somewhat unexpected because the experimental sequences of ISIs often show long transients corresponding to a strong cumulative refractoriness that builds up over many intervals as seen in Fig. 1 *A*. Naively, one would expect that such transients go along with a slow process that leads to correlations between intervals, that in turn affect the low-frequency limit of the power spectrum as follows (79):

$$S_{\mathrm{nonrenew}}(f = 0) = r_0 CV_T^2 \left(1 + 2 \sum_k \rho_k \right). \tag{43}$$

Here, $\rho_k = \mathrm{Covar}(T_i, T_{i+k}) / \mathrm{Var}(T_i)$ are the serial correlation coefficients that quantify correlations between ISIs lagged by an integer value k. Indeed, it was shown previously by (36) that stimulated HEK cells exhibit no statistically significant interval correlations. We address and resolve this apparent contradiction of a strong cumulative refractory period without significant interval correlations in a follow-up paper, where we extend the renewal model discussed here by an equation describing the depletion and slow refilling of the ER.

Dependence of the statistics on cluster number and cluster dynamics

So far, we have fixed the parameters of the clusters, i.e., their number, the rates etc. Here, we consider the effects of the mean and variance of the IPI and the number of clusters K on the mean and CV of the ISI.

The mean and variability of the IPIs in the cluster model are largely controlled by λ_{ref}, the transition rate between the refractory states. Increasing this parameter makes the IPIs shorter on average because the dwell time in the refractory states is shortened. The IPI for larger λ_{ref} will also be less regular because it is then dominated by the single exponentially distributed transition that corresponds to the opening of the cluster. What is the effect of an increase of λ_{ref} on the mean and CV of the ISI? In Fig. 9, *A* and *B* the mean ISI and CV both display a systematic decrease with the refractory rate. Hence, paradoxically, a more regular IPI leads to a more irregular ISI.

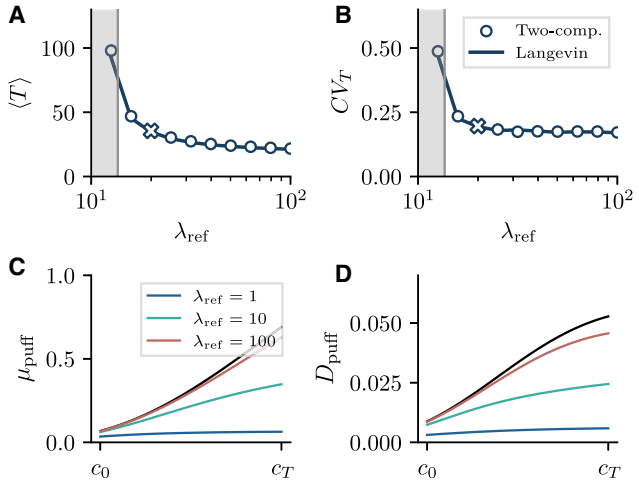

FIGURE 9 Spike-train statistics as functions of the refractory rate. (*A* and *B*) Show $\langle T \rangle$ and CV_T obtained from simulations of the two-component (*circle*) and Langevin model (*lines*), as functions of the refractory rate (the value $\lambda_{\mathrm{ref}} = 20\ \mathrm{s}^{-1}$ used so far is indicated by a *cross*). The refractory rate can be used to transition between the mean-driven and excitable regime (*gray area*). The mean ISI shows a systematic decrease as λ_{ref} increases while CV_T appears to saturate if the refractory rate is chosen sufficiently far away from the excitable regime. (*C* and *D*) Show the mean μ_{puff} and noise intensity D_{puff} of the puff current for three different values of the refractory rate. Note that both increase by a similar factor as λ_{ref} is increased and saturate for $\lambda_{\mathrm{ref}} \to \infty$ (*black line*). Hence, the decrease of the mean ISI as λ_{ref} increases stems from an increase of the mean and noise intensity of the puff current. Likewise the transition to the excitable regime stems from a decrease of the mean puff current. The saturation of the CV in (*B*) is reasonable if the model operates far from the bifurcation in the mean-driven regime and both the drift and noise intensity are scaled by similar factor as we argue in the main text. Parameters: $\tau = 5, p = 1.5 \times 10^{-2}, K = 10$. To see this figure in color, go online.

An explanation for the observed behavior can be given in terms of the mean puff current (Fig. 9, A_2 and *C*) and the noise intensity (Fig. 9, B_2 and *D*) with respect to different values of the refractory rate λ_{ref}. Let us first consider the case of a decreasing refractory rate corresponding to a more regular IPI. This leads to an overall decrease of both the mean puff current and noise intensity and also to a suppression of the Ca^{2+} feedback. This is so because for small refractory rates we face a system of clusters that spend most time in the Ca^{2+} insensitive refractory states. In this case the IF dynamics is dominated by the leak current and we may even enter the excitable regime (*gray area* in Fig. 9, B_1 and *B*) where spiking is rare and more irregular. Thus, the fact that the ISIs become more irregular when the IPIs become more regular is primarily due to the reduction of the mean puff current μ_{puff}.

In the opposite case of an increasing refractory rate, and hence stronger and more variable drive of the IF dynamics, the effect of this on the CV is less clear. In terms of the ISI variability a stronger drive results in more regular spiking, i.e., a smaller CV of the ISI. However, the simultaneous increase of the noise intensity has the opposite effect on the ISI variability, and, hence, it is not clear which of the two will win. However, we can resort to a simpler case to develop an intuition. If both the drift and the diffusion coefficient would not depend on c_{i} and would be scaled by the same factor (as is roughly the case [cf. Fig. 9, *C* and *D*], the CV would not change at all—this is the case of the so-called perfect IF model in neuroscience [see Eq. 20 in (78)] and further references therein). Indeed, if we start from our standard value at $\lambda_{\mathrm{ref}} = 20\ \mathrm{s}^{-1}$ (indicated by the *cross* in Fig. 9, *A* and *B*) and increase the refractory rate further, the CV does not change much in accordance to this reasoning. In conclusion, the more regular the IPI (the smaller λ_{ref}) the less regular the ISI.

Another dependence of interest concerns the number of clusters K, which may differ from cell to cell. A simple effect of increasing K is that the mean puff current and also the noise intensity increases in proportion to K, which is a consequence of the assumed statistical independence of the clusters. Both these increases will lead to shorter ISIs, as seen in Fig. 10 A_1. Again (comparable to the increase in λ_{ref} discussed above) the effect on the variability of the ISI is less clear because the increase in the mean and the increase in the noise intensity have opposing effects on the CV, at least in the mean-driven regime. Inline with the above argument, in Fig. 10 A_2 we see only small changes in the CV for a growing number of cluster. We note that for the parameters used here, we do not reach the excitable regime (again indicated by the *gray area* in

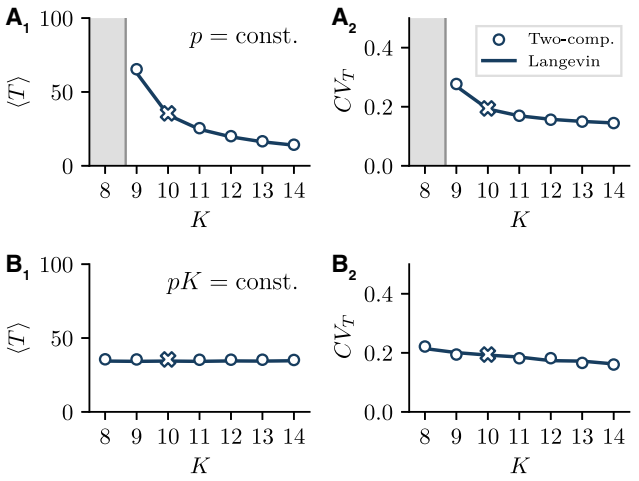

FIGURE 10 Spike-train statistics as functions of the number of clusters. In (*A*) we vary the number of clusters K and show $\langle T \rangle$ (A_1) and CV_T (A_2) obtained from simulations of the two-component (*circle*) and Langevin model (*lines*). The value $K = 10$ used so far is indicated by a cross. The mean ISI decreases as the number of clusters increases while the CV saturates. Similar as for the CV in Fig. 9, this is plausible if the model operates in the strongly mean-driven regime given that both the mean and noise intensity of the puff current depend linearly on K. In (*B*) we vary the number of clusters K but adjust p so that their product is fixed, $pK = \mathrm{const.}$ This results in a fixed mean puff current and decreasing noise intensity as K increases. Consequently, the mean $\langle T \rangle$ (B_1) is largely unaffected by the variation of K while the CV CV_T (B_2) scales as $1/\sqrt{K}$. Parameters: $\tau = 5$ (A): $p = 1.5 \times 10^{-2}$, (*B*) $p(K) = 1.5 \times 10^{-1}/K$. To see this figure in color, go online.

Fig. 10, A_1 and A_2) without entirely suppressing spiking. If we would reach the excitable regime (by changing other parameters), we would encounter much stronger increases in the CV comparable to what we have seen in Fig. 9 B_1 for small values of λ_{ref}.

Finally, we turn to a situation in which the cluster density is preserved while we increase K (Fig. 10, B_1 and B_2). This roughly corresponds to an increase in cell size which increases the number of clusters but decreases the change of the Ca^{2+} concentration such that the mean puff current is conserved. Accordingly, we study now a scaling in which $pK = \text{const.}$; the ISI statistics for this case are shown in Fig. 10, B_1 and B_2. Since the mean puff current does not change by construction, we see only very little change in the mean ISI in this case (Fig. 10 B_1). The dominating change in this scaling is a reduction of the noise intensity by $1/K$. This, however, has also only little effect on the CV (Fig. 10 B_2) because the relative change of the noise intensity remains small in the considered range of K. Because the system operates in the strongly mean-driven regime, again the scaling argument for the CV of an IF model with constant drift and constant diffusion (78) is meaningful; indeed the observed curve can be perfectly fitted by $CV_T \propto 1/\sqrt{K}$ (not shown).

Extension of the model by an additional fast Ca^{2+} buffer: Effects on the spiking train statistics

An important element in Ca^{2+} signaling that we have not taken into account so far, are buffer proteins that may bind up to 99% of the free Ca^{2+} both in the cytosol and ER (80,81). Here, we extend our model by an additional Ca^{2+} buffer and discuss how the mean and CV of the ISI are affected. The reaction scheme for the buffer B reads:

$$\mathrm{Ca}^{2} + \mathrm{B} \underset{k^+}{\overset{k^-}{\rightleftharpoons}} \mathrm{CaB}, \tag{44}$$

where k^+ and k^- are rate constants (often assumed to be large corresponding to a fast buffer) and the dissociation constant is given by $K^* = k^-/k^+$. The differential equations for the cytosolic Ca^{2+} *and* the fast buffer concentration can be formulated as follows:

$$\begin{aligned} \dot{c}_{\mathrm{i}} &= -(c_{\mathrm{i}} - c_0)/\tau + j_{\mathrm{puff}}(c_{\mathrm{i}}) - k^+ c_{\mathrm{i}}(b_T - c_b) + k^- c_b \\ \dot{c}_b &= k^+ c_{\mathrm{i}}(b_T - c_b) - k^- c_b \\ &\text{if } c_{\mathrm{i}}(t) = c_T \to t_i = t \text{ and } c_{\mathrm{i}}(t) = c_R, c_b(t) = c_b^0(c_R) \end{aligned} \tag{45}$$

where $b_T = b + c_b$ is the total buffer concentration given by the sum of the free and Ca^{2+}-bound buffer concentration b and c_b, respectively; we assume b_T to be constant in time. In an IF framework a fast buffer, that is always in equilibrium with the cytosolic Ca^{2+} concentration, requires an additional reset rule for the bound buffer concentration c_b. This condition is given in the last line of Eq. 45 and states that c_b is reset to the equilibrium value, $c_b^0(c_{\mathrm{i}}) = c_{\mathrm{i}} b_T/(K^* + c_{\mathrm{i}})$, taken at the reset $c_{\mathrm{i}} = c_R$. This reset rule ensures that c_b remains in equilibrium even after the infinitely fast reset of c_{i}. According to (82) a fast buffer can be eliminated and affects the dynamics of c_{i} only through a (c_{i} dependent) factor β:

$$\begin{aligned} \frac{dc_i}{dt} &= \beta\left[-(c_{\mathrm{i}} - c_0)/\tau + j_{\mathrm{puff}}(c_{\mathrm{i}})\right], \\ \beta &= \left(1 + K^* b_T/(K^* + c_{\mathrm{i}})^2\right)^{-1}. \end{aligned} \tag{46}$$

Assuming that the c_{i} dependence of β is weak ($K^* \gg c_{\mathrm{i}}$) one could wrongly conclude that adding a fast Ca^{2+} buffer simply leads to a rescaling of the time, hence affects the mean but not the CV of the ISIs. However, this is not true. To make this clear consider the Langevin approximation of Eq. 46 and substitute $t = \hat{t}/\beta$. Considering the dynamics with respect to this new time leads to a deterministic drift that is independent of β but a noise intensity that is not:

$$\frac{dc_{\mathrm{i}}}{d\hat{t}} = f(c_{\mathrm{i}}) + \sqrt{2\beta D_{\mathrm{puff}}(c_{\mathrm{i}})}\,\xi(\hat{t}), \tag{47}$$

due to the scaling properties of the white noise $\sqrt{\beta}\xi(\hat{t}) = \xi(\hat{t}/\beta)$. (Rescaling the time $t = \hat{t}/\beta$ of a white noise process affects its intensity because the autocorrelation function should be preserved, i.e., $2D\delta(t - t') = 2D^*\delta(\hat{t} - \hat{t}')$. Using the scaling property of the Dirac delta function $\delta((\hat{t} - \hat{t}')/\beta) = |\beta|\delta(\hat{t} - \hat{t}')$ allows to relate the two intensities $D^* = \beta D$ so that one finds $\sqrt{\beta}\xi(\hat{t}) = \xi(\hat{t}/\beta)$.)

In the mean-driven regime the average ISI depends strongly on the drift but only weakly on the noise intensity. Because in the rescaled time the drift does not depend on β, this implies that average ISI in the rescaled dynamics is also independent of β. Going back to the original time, intervals scale linearly with $1/\beta$ as time itself:

$$\langle T \rangle \approx \langle T_0 \rangle / \beta \approx \langle T_0 \rangle (1 + b_T / K^*) \tag{48}$$

where $\langle T_0 \rangle$ refers to the mean ISI measured in units of $\hat{t}$ or, equivalently, to the mean ISI measured in units of t but without a buffer, $b_T = 0$. If we further assume that $b_T/K^* \gg 1$, Eq. 48 implies an approximately linear relationship between $\langle T \rangle$ and the total buffer concentration b_T. In Fig. 11 A_1 we demonstrate this linear relation, Eq. 48 (*red line*), by means of stochastic simulations of the two-component model with an additional buffer according to Eq. 45 (*circles*). We also compare this to the Langevin approximation of the same model version, i.e., Eq. 45 where the puff current is substituted according to Eq. 32 (*blue line*). The two stochastic simulation results agree well with each other; however, they display a slightly slower but still linear increase compared with the simple estimate Eq. 48.

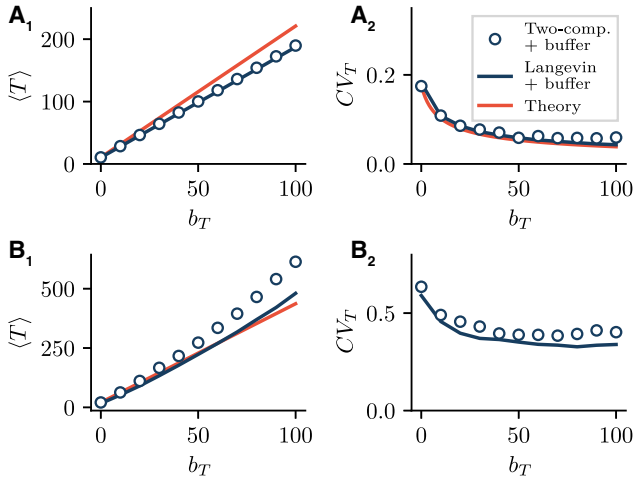

FIGURE 11 Spike-train statistics as functions of the total buffer concentration. (*A* and *B*) The model is in the mean-driven and excitable regime, respectively. (A_1 and B_1) Show $\langle T \rangle$ while (A_2 and B_2) show CV_T, both obtained from simulations of the two-component (*circle*) and Langevin model (*lines*) with an additional fast buffer according to Eq. 45 as a function of the total buffer concentration b_T. In the mean-driven regime the mean ISI (A_1) is linear in b_T according to Eq. 48 and the CV (A_2) depends on b_T as given in Eq. 50. In the excitable regime the mean ISI (B_1) that depends superlinearly on b_T deviating somewhat from the theoretical prediction (*red line*) and the Langevin simulation (*blue line*). The CV (B_2) in the excitable regime is robust over a large range of buffer concentrations. Parameters: $K = 10$, $k^+ = 10$, $k^- = 50$, (*A*): $\tau = 5$, $p = 2.5 \times 10^{-2}$, (*B*): $\tau = 1$, $p = 6.4 \times 10^{-2}$. To see this figure in color, go online.

The effect of a fast buffer on the CV is more complicated. However, when the system is in the mean-driven regime and the noise intensity is not too strong, the influence of the buffer concentration on the variance of the ISIs can be estimated according to (83):

$$\langle \Delta T^2 \rangle = 2\beta \int_{c_0}^{c_T} dc_i \, D_{\text{puff}}(c_i) \, / f(c_i)^3, \qquad (49)$$

where we have again assumed that β is independent of c_i. The CV is then given by:

$$CV_T \approx \frac{\sqrt{\langle \Delta T_0^2 \rangle / \beta}}{\langle T_0 \rangle / \beta} \approx \frac{CV_{T,0}}{\sqrt{(1 + b_T/K^*)}}, \qquad (50)$$

where $CV_{T,0}$ refers to the CV without a buffer. The CV thus exhibits a simple square-root relation with respect to the total buffer concentration that is confirmed in Fig. 11 A_2.

In Fig. 11, B_1 and B_2 we consider a scenario where spiking is fluctuation driven (excitable regime) and the mean interval therefore depends more strongly on the noise intensity and in turn buffer concentration. In particular, the mean interval obtained from stochastic simulations of the two-component model with a buffer grows faster than linear (cf. *circles* in Fig. 11 B_1). This is so because in the excitable regime the passage to the threshold is facilitated by noise—in addition to diminishing the drift we now also diminish the intensity of the noise by increasing b_T, which leads to a superlinear increase of the mean interval with b_T. Interestingly, for the Langevin approximation this superlinear growth is less pronounced, which is in line with the fact that this approximation works less well in the excitable regime. The variability of the ISIs also drops with b_T; apparently we are here far from the weak-noise limit where the CV can decrease upon a reduction of the noise intensity (we are on the r.h.s. of the coherence-resonance minimum, see (73)).

SUMMARY AND DISCUSSION

This study exploited the similarities between stochastic spike generation in neural dynamics and in Ca^{2+} dynamics to develop a phenomenological but biophysically grounded model of Ca^{2+} spiking and used established methods from computational neuroscience to calculate spike train statistics analytically. The main source of variability is the Ca^{2+} noise generated by the stochastic opening of clusters of IP_3R channels in the ER membrane leading to stochastic sequence of Ca^{2+} release puffs. This *cluster noise* is similar to the ion channel noise in the membrane potential dynamics of neurons and can be treated mathematically in a similar way, i.e., by a diffusion approximation. Furthermore, for a simplified description of intracellular Ca^{2+} spiking, we have adopted the IF framework of computational neuroscience. Our resulting two-component model captures the punctuated release of Ca^{2+} from IP_3Rs on the one hand and the dynamics of the cytosolic Ca^{2+} on the other hand. It can reproduce the spike statistics of HEK cells, ranging from Fano factors to spike train power spectra quantitatively (see Fig. 8).

Specifically, we suggested a phenomenological puff model which meets a variety of experimentally observed puff characteristics. Five observations have been used to design the model: 1) puffs occur randomly (see Yao et al. (84)); 2) the amplitude is uniformly distributed over the number of channels in the cluster (see Dickinson and Parker (50)); 3) dwell times in a cluster state with a given number of open channels are rather independent of that number (see Wiltgen et al. (52)); 4) IPIs may exhibit a refractory period (see Thurley et al. (45)), and 5) the approximate values of the IPI's mean and refractory period (see Thurley et al. (45)). For the resulting Markov model of the cluster activity we provide expressions for the mean (Eq. 18a) and CV (Eq. 18c) of the IPI as well as the mean (Eq. 13) and CV (Eq. 15) of the puff strength. The CV of the IPI at the resting Ca^{2+} concentration resulting from this model is close to 1 with parameters chosen according to Fig. 2, and in agreement with low stimulation results for HEK cells (45), which is our standard example here. SHSY-5Y cells exhibit a CV of 0.68 at low and of 0.42 at high stimulation (45), which can also be modeled by adjusting the cluster parameters accordingly (Eq. 18c admits arbitrarily low CVs if we add a sufficient number of refractory states; it holds specifically that $\lim_{M\to\infty} CV_I = 0$), cf. Eq. 18c).

Puff activity is one of the currents contributing to the global Ca^{2+} dynamics. Here, we have shown that because of the timescale separation between the puff dynamics and the cytosolic Ca^{2+} dynamics the puff current can be well approximated by a white Gaussian noise with a Ca^{2+}-dependent mean and Ca^{2+}-dependent noise intensity, functions, which can be calculated from the transition rate matrix according to Eq. 22 and Eq. 28, respectively. This diffusion approximation provides a simple method to determine the Langevin equation corresponding to a given channel cluster model. That might also find applications to models of cardiomyocytes and their Ca^{2+} release units.

The derived Langevin approximation for the dynamics of the cytosolic Ca^{2+} concentration permits stochastic simulations that are by orders of magnitude faster than the simulation of the full two-component model. It furthermore allows to distinguish in a simple manner the mean-driven and the excitable regimes. Moreover, in this approximation, different ISI statistics can be calculated analytically, i.e., we can find quadrature expressions for the mean and variance of the ISI and, at least in the mean-driven regime, also simple estimates for the ISI density and spike-train power spectrum. We have also shown that the interpretation of the stochastic differential equation with multiplicative noise (Ito-Stratonovich dilemma (60,67)) is not a major issue for the biophysically relevant parameter range.

Beside validating our approximation we also explored the dependence of the ISI statistics on the biophysical parameters of the cell (the time constant of the leak current τ and permeability-like parameter p) and the clusters (their number K and refractory rate λ_{ref}). We have shown that the model in either the mean-driven or excitable regimes can reproduce experimentally measured CV values which range from 0.2 in Vasporessin-stimulated Hepatocytes to 1.0 in spontaneously spiking Astrocytes (10,14,85–87). As already mentioned above, we demonstrated that our model can generate spike trains with statistics highly similar to those of stimulated HEK cells.

Finally, motivated by the experimental results by Skupin et al. (10) we also investigated the effect of incorporating a fast Ca^{2+} buffer in our model. Here, we find an approximately linear scaling of the mean ISI with the total buffer concentration and in particular the scaling $\langle T\rangle \propto 1 + b_T/K^*$ in the mean-driven regime, i.e., the model reproduces the experimentally observed increase of the mean ISI with increasing buffer concentration (10). Note that the total buffer concentration b_T takes into account Ca^{2+} binding proteins that are naturally present in the cell and hence does not directly corresponds to the concentration of the added buffer. Another remarkable experimental finding by Skupin and Falcke (88) was that the CV is largely independent of the concentration of the added buffer. This feature is consistent with our model if it operates in the excitable regime close to the bifurcation Fig. 11 B_2 and we include an offset in the buffer concentration.

As an outlook we note that the CV of experimental spike trains exhibits robustness against cell-to-cell variability. Parameters describing cell variability are the number of clusters and variability of the strength of cluster-to-cluster coupling due to the variable geometry of the cluster array. We have shown that, at least in a scenario with fixed cluster density, our model's CV is largely independent of the number of clusters. Additional robustness of the CV is likely to arise from a slow recovery from negative feedback which terminated the previous spike, i.e., spike generation happens in a transient (20,89). This transient is assumed to provide the CV robustness properties. We expect that adding such a transient to the Langevin formulation would entail the observed robustness properties. This is studied in a follow-up paper to the study presented here.

Appendix

Mean and variance of the surrogate random process $Y(t)$

Here, we relate the mean μ_Y and variance σ_Y^2 of the coarse-grained random process $Y(t)$ defined by Eq. 30 to the mean μ_x and noise intensity D_x of the single cluster $x(t)$ under the assumption that c_{i} changes slowly. The means can be readily related to one another using that the mean of a sum of random numbers is the sum of their means. This yields the expression:

$$\begin{aligned}\mu_Y &= \langle Y(t;\Delta t)\rangle = \frac{1}{\Delta t}\int_t^{t+\Delta t} dt_1 \left\langle \sum_k^K x_k(t_1)\right\rangle \\ &= \frac{1}{\Delta t}\int_t^{t+\Delta t} dt_1 \quad K\langle x(t_1)\rangle \\ &= K\mu_x,\end{aligned} \tag{51}$$

that holds irrespective of any timescale separation.

Relating the variance to the noise intensity of a single cluster is more complicated because it requires that the correlation function of a single cluster decays sufficiently fast. The variance of $Y(t)$ is given by:

$$\begin{aligned}\sigma_Y^2 &= \left\langle \Delta Y(t;\Delta t)^2\right\rangle \\ &= \frac{1}{\Delta t^2}\iint_t^{t+\Delta t} dt_1 dt_2 \sum_{k_1=1}^K \sum_{k_2=1}^K \langle \Delta x_{k_1}(t_1)\Delta x_{k_2}(t_2)\rangle, \\ &= \frac{1}{\Delta t^2}\iint_t^{t+\Delta t} dt_1 dt_2 \left[\sum_{k_1=1}^K \langle \Delta x_{k_1}(t_1)\Delta x_{k_1}(t_2)\rangle \right. \\ &\qquad \left. + \sum_{k_1\neq k_2}^K \langle \Delta x_{k_1}(t_1)\Delta x_{k_2}(t_2)\rangle\right], \\ &= \frac{K}{\Delta t^2}\iint_t^{t+\Delta t} dt_1 dt_2 \; C_{xx}(t_2 - t_1).\end{aligned} \tag{52}$$

To get from the second to the third line we have 1) used that the clusters are independent of one another so that the covariance $\langle \Delta x_{k_1}(t_1)\Delta x_{k_2}(t_2)\rangle$ vanishes and 2) introduced the autocorrelation function $C_{xx}(t_2 - t_1) = \langle \Delta x(t_2)\Delta x(t_1)\rangle$ with $\Delta x = x - \langle x\rangle$. This expression can be further simplified (very similar to the derivation of the Kubo relation (90)) using that the autocorrelation only depends on the difference $\tau = t_2 - t_1$ and is symmetric $C_{xx}(\tau) = C_{xx}(-\tau)$:

$$\begin{aligned}\sigma_Y^2 &= \frac{K}{\Delta t^2}\int_t^{t+\Delta t}\int dt_1 dt_2\, C_{xx}(t_2 - t_1)\\ &= \frac{2K}{\Delta t}\int_0^{\Delta t} d\tau\, C_{xx}(\tau)(1 - \tau/\Delta t).\end{aligned} \tag{53}$$

Hence, the autocorrelation function of $x(t)$ determines the variance of the surrogate random process $Y(t)$. This expression can be related to the noise intensity of the puff current through a single cluster:

$$D_x = \int_0^\infty d\tau \quad C_{xx}(\tau) \tag{54}$$

if, in line with our initial assumption, the correlation time τ_Y is assumed to be small compared with the time-window Δt. In this case the term $\tau/\Delta t$ in Eq. 53 can be neglected so that we find:

$$\sigma_Y^2 = \frac{2KD_x}{\Delta t}. \tag{55}$$

Stationary probability density and firing rate

The derived Langevin equation Eq. 33 can be used to calculate the stationary probability density function $p_0(c_i)$ and the firing rate $r_0 = 1/\langle T\rangle$. To this end, we need to establish the associated FPE (32,69–71) that was already given in the main part and is repeated here for convenience:

$$\begin{aligned}\partial_t p(c_i,t) = {}& \partial_{c_i}[-f(c_i) - D'(c_i)/2 + \partial_{c_i}D(c_i)]p(c_i,t)\\ &+ r_0\delta(c_i - c_R),\end{aligned} \tag{56}$$

with the drift term $f(c_i) = -(c_i - c_0)/\tau + \mu_{\text{puff}}(c_i)$ and the noise-induced Stratonovich drift $D'(c_i)/2$. The FPE is completed by the natural boundary condition $p(c_i \to -\infty, t) = 0$, absorbing boundary condition $p(c_T,t) = 0$ and normalization $\int dc_i\, p(c_i,t) = 1$. We first calculate the stationary firing rate r_0 by means of the stationary probability density function $p_0(c_i)$ of Eq. 56:

$$\begin{aligned}0 = {}& [-f(c_i) - D'(c_i)/2 + \partial_{c_i}D(c_i)]p_0(c_i)\\ &+ r_0\Theta(c_i - c_R),\end{aligned} \tag{57}$$

where we have dropped the time derivative because we are interested in the stationary case and integrated once with respect to c_i. To solve this equation we introduce two auxiliary functions $L(c_i) = D(c_i)p_0(c_i)$ and define $g(c_i) = f(c_i) + D'(c_i)/2$ and obtain:

$$\partial_{c_i}L(c_i) = \frac{g(c_i)}{D(c_i)}L(c_i) - r_0\Theta(c_i - c_R), \tag{58}$$

the homogeneous solution $L_h(c_i)$ to this equation is readily obtained:

$$L_h(c_i) \propto \exp\left(\int_{c_R}^{c_i} dy\frac{g(y)}{D(y)}\right). \tag{59}$$

The method of variation of parameters yields the full solution:

$$\begin{aligned}L(c_i) &= r_0 e^{h(c_i)}\int_{c_i}^{c_T} dx\, e^{-h(x)}\Theta(x - c_R),\\ h(x) &= \int_{c_R}^{x} dy\,\frac{g(y)}{D(y)}.\end{aligned} \tag{60}$$

Finally, we substitute the probability density $p_0(c_i)$ again and find:

$$P_0(c_i) = r_0\frac{e^{h(c_i)}}{D(c_i)}\int_{c_i}^{c_T} dx\, e^{-h(x)}\Theta(x - c_R) \tag{61}$$

Note that the desired firing rate r_0 can be obtained by means of the normalization condition, put differently we can integrate over c_i from $-\infty$ to and obtain:

$$r_0 = \left(\int_{c_R}^{c_T} dc_i\, e^{-h(c_i)}\int_{-\infty}^{c_i} dx \quad \frac{e^{h(x)}}{D(x)}\right)^{-1} \tag{62}$$

For this expression we have used that the boundaries of the integral can be interchanged as follows:

$$\begin{aligned}&\int_{-\infty}^{x_T} dx_1\int_{x_1}^{x_T} dx_2\, f(x_1,x_2)\theta(x_2 - x_R)\\ &\quad = \int_{x_R}^{x_T} dx_2\int_{-\infty}^{x_2} dx_1\, f(x_1,x_2).\end{aligned} \tag{63}$$

Coefficient of variation

The CV $CV_T^2 = \langle \Delta T^2\rangle/\langle T\rangle^2$ can be calculated by considering the ISI T as a first-passage time (FPT). Put differently, we consider a "particle" governed by Eq. 33 with $c_i(T = 0) = c_0$ and ask what the distribution of times is at which it will first cross the threshold c_T. This is the so-called FPT density $p_{\text{FP}}(T)$ that itself is usually not analytical accessible but its moments $\langle T^n\rangle$ are (59). To calculate the moments, we establish the respective FPE (see, e.g., (91)):

$$\begin{aligned}\partial_T p(c_i,T) &= \partial_{c_i}[-f(c_i) - D'(c_i)/2 + \partial_{c_i}D(c_i)]p(c_i,T)\\ &= -\partial_{c_i}j(c_i,T)\end{aligned} \tag{64}$$

with the probability current $j(c_i,T)$. The boundary and initial conditions are given by:

$$p(-\infty,T) = p(c_T,T) = 0, \quad p(c_i,0) = \delta(c_i - c_0). \tag{65}$$

Note that in contrast to Eq. 56 this FPE does not posses any source terms that correspond to the reset rule of Eq. 33. This is so because for the *first*-passage time, trajectories that have crossed the threshold are not reset but absorbed. An important insight is that the FPT density is given by the probability current evaluated at the threshold:

$$p_{\mathrm{FP}}(T) = j(c_T,T). \tag{66}$$

Calculating the moments of FPT density is, in the one-component case, a standard problem in the theory of stochastic processes (59). Here, we do not present the full derivation but refer to (91) and specifically to the hierarchy of differential equations that determines the moments:

$$-nJ_{n-1}(c_i) = -g(c_i)J_n'(c_i) + \partial_{c_i}D(c_i)J_n'(c_i), n > 0. \tag{67}$$

Here, $J_n(c_T) = \langle T^n \rangle$ are exactly the moments of the FPT density and $J_0(c_i) = \Theta(c_i - c_0)$. The generalization to the case of multiplicative noise is straightforward. The solution to the second moment is given by:

$$\langle T^2 \rangle = 2\int_{c_R}^{c_T} dx_4\, e^{-h(x_4)} \int_{-\infty}^{x_4} dx_3\, \frac{e^{h(x_3)}}{D(x_3)} \times \int_{x_3}^{c_T} dx_2\, e^{-h(x_2)} \int_{-\infty}^{x_2} dx_1\, \frac{e^{h(x_1)}}{D(x_1)} \tag{68}$$

with $h(x)$ as in Eq. 60. The evaluation of these four nested integrals is challenging, even numerically. Luckily, in case of the variance the expression can be simplified greatly to contain only two nested integrals (cf. (70)):

$$\langle \Delta T^2 \rangle = 2\int_{-\infty}^{c_T} dx_3\, e^{-h(x_3)} \left(\int_{-\infty}^{x_3} dx_2\, \frac{e^{h(x_2)}}{D(x_2)} \right)^2 \times \int_{x_3}^{c_T} dx_1\, e^{-h(x_1)} \Theta(x_1 - c_R). \tag{69}$$

AUTHOR CONTRIBUTIONS

The authors confirm contribution to the paper as follows: Methodology, software, investigation, data curation, writing, and visualization, L.R.; conceptualization, methodology, validation, investigation, writing, supervision, and project administration, B.L.; conceptualization, writing – review & editing, supervision, and project administration, M.F. All authors reviewed the results and approved the final version of the manuscript.

ACKNOWLEDGMENTS

We thank V.N. Friedhoff, Max Delbrück Center Berlin, for stimulating discussions, and A. Skupin, University of Luxembourg, and K. Thurley, University Bonn, for providing HEK cell data. L.R. and B.L. acknowledges support by grant LI 1046/4-1 from the Deutsche Forschungsgemeinschaft. M.F. acknowledges support by grant FA 350/13-1 from the Deutsche Forschungsgemeinschaft.

DECLARATION OF INTERESTS

The authors declare no competing interests.

REFERENCES

1. Berridge, M. J., P. Lipp, and M. D. Bootman. 2000. The versatility and universality of calcium signalling. *Nat. Rev. Mol. Cell Biol.* 1:11–21.
2. Berridge, M. J., M. D. Bootman, and H. L. Roderick. 2003. Calcium signalling: Dynamics, homeostasis and remodelling. *Nat. Rev. Mol. Cell Biol.* 4:517–529.
3. Schipke, C. G., A. Heidemann, …, H. Kettenmann. 2008. Temperature and nitric oxide control spontaneous calcium transients in astrocytes. *Cell Calcium.* 43:285–295.
4. Thul, R., T. C. Bellamy, …, S. Coombes. 2009. Calcium oscillations. *In* Cellular Oscillatory Mechanisms. Advances in Experimental Medicine and Biology, *641*. M. Maroto and N. A. M. Monk, eds Springer New York, pp. 1–27.
5. Clapham, D. E. 2007. Calcium signaling. *Cell.* 131:1047–1058.
6. Campbell, K. A. 2014. Intracellular Calcium. John Wiley & Sons.
7. Shuai, J. W., and P. Jung. 2002. Optimal intracellular calcium signaling. *Phys. Rev. Lett.* 88:068102.
8. Shuai, J. W., and P. Jung. 2002. Stochastic properties of Ca^{2+} release of inositol 1,4,5-trisphosphate receptor clusters. *Biophys. J.* 83:87–97.
9. Shuai, J. W., and P. Jung. 2003. Optimal ion channel clustering for intracellular calcium signaling. *Proc. Natl. Acad. Sci. USA.* 100:506–510.
10. Skupin, A., H. Kettenmann, …, M. Falcke. 2008. How does intracellular Ca^{2+} oscillate: By chance or by the clock? *Biophys. J.* 94:2404–2411.
11. Perc, M., A. K. Green, …, M. Marhl. 2008. Establishing the stochastic nature of intracellular calcium oscillations from experimental data. *Biophys. Chem.* 132:33–38.
12. Dupont, G., A. Abou-Lovergne, and L. Combettes. 2008. Stochastic aspects of oscillatory Ca^{2+} dynamics in hepatocytes. *Biophys. J.* 95:2193–2202.
13. Jung, P., D. Swaminathan, and A. Ullah. 2010. Calcium spikes: Chance or necessity? *Chem. Phys.* 375:625–629, Stochastic processes in Physics and Chemistry (in honor of Peter Hänggi).
14. Thurley, K., S. C. Tovey, …, M. Falcke. 2014. Reliable encoding of stimulus intensities within random sequences of intracellular Ca^{2+} spikes. *Sci. Signal.* 7:ra59.
15. Croft, W., K. Reusch, …, T. C. Bellamy. 2016. Probabilistic encoding of stimulus strength in astrocyte global calcium signals. *Glia.* 64:537–552.
16. Tilūnaitė, A., W. Croft, …, R. Thul. 2017. A Bayesian approach to modelling heterogeneous calcium responses in cell populations. *PLoS Comput. Biol.* 13:e1005794.
17. Powell, J., M. Falcke, …, R. Thul. 2020. A statistical view on calcium oscillations. *In* Advances in Experimental Medicine and Biology, *1131* Springer International Publishing, pp. 799–826.
18. Skupin, A., H. Kettenmann, and M. Falcke. 2010. Calcium signals driven by single channel noise. *PLoS Comput. Biol.* 6:e1000870.
19. Calabrese, A., D. Fraiman, …, S. Ponce Dawson. 2010. Stochastic fire-diffuse-fire model with realistic cluster dynamics. *Phys. Rev. E Stat. Nonlin. Soft Matter Phys.* 82:031910. https://doi.org/10.1103/PhysRevE.82.031910.
20. Thurley, K., and M. Falcke. 2011. Derivation of Ca2+ signals from puff properties reveals that pathway function is robust against cell

variability but sensitive for control. *Proc. Natl. Acad. Sci. USA.* 108:427–432.

21. Rüdiger, S. 2014. Stochastic models of intracellular calcium signals. *Phys. Rep.* 534:39–87.
22. Dupont, G., M. Falcke, …, J. Sneyd. 2016. Models of calcium signalling. *In* Interdisciplinary Applied Mathematics, *43* Springer.
23. Burkitt, A. N. 2006. A review of the integrate-and-fire neuron model: I. Homogeneous synaptic input. *Biol. Cybern.* 95:1–19.
24. Burkitt, A. N. 2006. A review of the integrate-and-fire neuron model: II. Inhomogeneous synaptic input and network properties. *Biol. Cybern.* 95:97–112.
25. Vilela, R. D., and B. Lindner. 2009. A comparative study of three different integrate-and-fire neurons: Spontaneous activity, dynamical response, and stimulus-induced correlation. *Phys. Rev. E Stat. Nonlin. Soft Matter Phys.* 80:031909.
26. Gerstner, W., W. M. Kistler, …, L. Paninski. 2014. Neuronal Dynamics from Single Neurons to Networks and Models of Cognition. Cambridge University Press.
27. Friedhoff, V. N., L. Ramlow, …, M. Falcke. 2021. Models of stochastic Ca^{2+} spiking. *Eur. Phys. J. Spec. Top.* 230:2911–2928.
28. Jolivet, R., F. Schürmann, …, A. Roth. 2008. The quantitative single-neuron modeling competition. *Biol. Cybern.* 99:417–426.
29. Badel, L., S. Lefort, …, M. J. E. Richardson. 2008. Dynamic I-V curves are reliable predictors of naturalistic pyramidal-neuron voltage traces. *J. Neurophysiol.* 99:656–666.
30. Ricciardi, L. M. 1977. Diffusion Processes and Related Topics on Biology. Springer-Verlag.
31. Tuckwell, H. C. 1989. Stochastic Processes in the Neuroscience. SIAM.
32. Fourcaud, N., and N. Brunel. 2002. Dynamics of the firing probability of noisy integrate-and-fire neurons. *Neural Comput.* 14:2057–2110.
33. Droste, F., and B. Lindner. 2014. Integrate-and-fire neurons driven by asymmetric dichotomous noise. *Biol. Cybern.* 108:825–843.
34. Schwalger, T., F. Droste, and B. Lindner. 2015. Statistical structure of neural spiking under non-Poissonian or other non-white stimulation. *J. Comput. Neurosci.* 39:29–51.
35. Ramlow, L., and B. Lindner. 2021. Interspike interval correlations in neuron models with adaptation and correlated noise. *PLoS Comput. Biol.* 17:e1009261.
36. Skupin, A., and M. Falcke. 2010. Statistical analysis of calcium oscillations. *Eur. Phys. J. Spec. Top.* 187:231–240.
37. Lock, J. T., and I. Parker. 2020. IP_3 mediated global Ca^{2+} signals arise through two temporally and spatially distinct modes of Ca^{2+} release. *Elife.* 9:e55008.
38. Vorontsova, I., J. T. Lock, and I. Parker. 2022. KRAP is required for diffuse and punctate IP_3-mediated Ca^{2+} liberation and determines the number of functional IP_3R channels within clusters. *Cell Calcium.* 107:102638.
39. Sneyd, J., M. Falcke, …, C. Fox. 2004. A comparison of three models of the inositol trisphosphate receptor. *Prog. Biophys. Mol. Biol.* 85:121–140.
40. De Young, G. W., and J. Keizer. 1992. A single-pool inositol 1,4,5-trisphosphate-receptor-based model for agonist-stimulated oscillations in Ca^{2+} concentration. *Proc. Natl. Acad. Sci. USA.* 89:9895–9899.
41. Gin, E., M. Falcke, …, J. Sneyd. 2009. A kinetic model of the inositol trisphosphate receptor based on single-channel data. *Biophys. J.* 96:4053–4062.
42. Siekmann, I., L. E. Wagner, 2nd, …, J. Sneyd. 2012. A kinetic model for type I and II IP_3R accounting for mode changes. *Biophys. J.* 103:658–668.
43. Higgins, E. R., H. Schmidle, and M. Falcke. 2009. Waiting time distributions for clusters of IP_3 receptors. *J. Theor. Biol.* 259:338–349.
44. Shuai, J., J. E. Pearson, …, I. Parker. 2007. A kinetic model of single and clustered IP_3 receptors in the absence of Ca^{2+} feedback. *Biophys. J.* 93:1151–1162.
45. Thurley, K., I. F. Smith, …, M. Falcke. 2011. Timescales of IP_3-evoked Ca^{2+} spikes emerge from Ca^{2+} puffs only at the cellular level. *Biophys. J.* 101:2638–2644.
46. Lock, J. T., I. F. Smith, and I. Parker. 2017. Comparison of Ca2+ puffs evoked by extracellular agonists and photoreleased IP3. *Cell Calcium.* 63:43–47, Calcium Signaling: from Stores to Channels. Honoring James W. Putney Jr. https://www.sciencedirect.com/science/article/pii/S0143416016301877.
47. Lock, J. T., K. J. Alzayady, …, I. Parker. 2018. All three IP_3 receptor isoforms generate Ca^{2+} puffs that display similar characteristics. *Sci. Signal.* 11:eaau0344.
48. Bezprozvanny, I., J. Watras, and B. E. Ehrlich. 1991. Bell-shaped calcium-response curves of $Ins(1,4,5)P_3$-and calcium-gated channels from endoplasmic reticulum of cerebellum. *Nature.* 351:751–754.
49. Smith, I. F., and I. Parker. 2009. Imaging the quantal substructure of single IP_3R channel activity during Ca^{2+} puffs in intact mammalian cells. *Proc. Natl. Acad. Sci. USA.* 106:6404–6409.
50. Dickinson, G. D., and I. Parker. 2013. Factors determining the recruitment of inositol trisphosphate receptor channels during calcium puffs. *Biophys. J.* 105:2474–2484.
51. Dickinson, G. D., D. Swaminathan, and I. Parker. 2012. The probability of triggering calcium puffs is linearly related to the number of inositol trisphosphate receptors in a cluster. *Biophys. J.* 102:1826–1836.
52. Wiltgen, S. M., G. D. Dickinson, …, I. Parker. 2014. Termination of calcium puffs and coupled closings of inositol trisphosphate receptor channels. *Cell Calcium.* 56:157–168.
53. Bentele, K., and M. Falcke. 2007. Quasi-steady approximation for ion channel currents. *Biophys. J.* 93:2597–2608.
54. Foskett, J. K., C. White, …, D. O. D. Mak. 2007. Inositol trisphosphate receptor Ca^{2+} release channels. *Physiol. Rev.* 87:593–658.
55. Rossi, A. M., S. C. Tovey, …, C. W. Taylor. 2012. Analysis of IP_3 receptors in and out of cells. *Biochim. Biophys. Acta.* 1820:1214–1227.
56. Mak, D. O., S. McBride, and J. K. Foskett. 1998. Inositol 1,4,5-trisphosphate activation of inositol tris-phosphate receptor Ca^{2+} channel by ligand tuning of Ca^{2+} inhibition. *Proc. Natl. Acad. Sci. USA.* 95:15821–15825.
57. Cao, P., M. Falcke, and J. Sneyd. 2017. Mapping interpuff interval distribution to the properties of inositol trisphosphate receptors. *Biophys. J.* 112:2138–2146.
58. Ross, S. 2010. A First Course in Probability. Pearson.
59. Gardiner, C. W. 1985. Handbook of Stochastic Methods. Springer-Verlag.
60. van Kampen, N. G. 1992. Stochastic Processes in Physics and Chemistry. North-Holland.
61. Risken, H. 1989. The Fokker-Planck Equation, second edition. Springer.
62. Lindner, B. 2007. The diffusion coefficient of nonlinear Brownian motion. *New J. Phys.* 9:136.
63. Lindner, B. 2008. Diffusion coefficient of a Brownian particle with a friction function given by a power law. *J. Stat. Phys.* 130:523–533.
64. Wang, X., Y. Hao, …, G. D. Smith. 2015. Ca^{2+}-activation kinetics modulate successive puff/spark amplitude, duration and inter-event-interval correlations in a Langevin model of stochastic Ca^{2+} release. *Math. Biosci.* 264:101–107.
65. Risken, H. 1984. The Fokker-Planck Equation. Springer.
66. van Kampen, N. G. 1981. Itô versus Stratonovich. *J. Stat. Phys.* 24:175–187.
67. Sokolov, I. M. 2010. Itô, Stratonovich, Hänggi and all the rest: the thermodynamics of interpretation. *Chem. Phys.* 375:359–363.
68. Wong, E., and M. Zakai. 1965. On the convergence of ordinary integrals to stochastic integrals. *Ann. Math. Statist.* 36:1560–1564.
69. Abbott, L., and C. van Vreeswijk. 1993. Asynchronous states in networks of pulse-coupled oscillators. *Phys. Rev. E Stat. Phys. Plasmas Fluids Relat. Interdiscip. Topics.* 48:1483–1490.

70. Lindner, B. 2002. Coherence and Stochastic Resonance in Nonlinear Dynamical Systems. Logos-Verlag.

71. Richardson, M. J. E. 2004. Effects of synaptic conductance on the voltage distribution and firing rate of spiking neurons. *Phys. Rev. E Stat. Nonlin. Soft Matter Phys.* 69:051918.

72. Cox, D. R. 1962. Renewal Theory. Methuen.

73. Lindner, B., J. García-Ojalvo, …, L. Schimansky-Geier. 2004. Effects of noise in excitable systems. *Phys. Rep.* 392:321–424.

74. Izhikevich, E. M. 2007. Dynamical Systems in Neuroscience: The Geometry of Excitability and Bursting. The MIT Press.

75. Middleton, J. W., M. J. Chacron, …, A. Longtin. 2003. Firing statistics of a neuron model driven by long-range correlated noise. *Phys. Rev. E Stat. Nonlin. Soft Matter Phys.* 68:021920.

76. Stratonovich, R. L. 1967. Topics in the Theory of Random Noise. Gordon and Breach.

77. Skupin, A., and M. Falcke. 2009. From puffs to global Ca^{2+} signals: How molecular properties shape global signals. *Chaos.* 19:037111.

78. Vilela, R. D., and B. Lindner. 2009. Are the input parameters of white-noise-driven integrate and fire neurons uniquely determined by rate and CV? *J. Theor. Biol.* 257:90–99.

79. Cox, D. R., and P. A. W. Lewis. 1966. The Statistical Analysis of Series of Events. Chapman and Hall.

80. Allbritton, N. L., T. Meyer, and L. Stryer. 1992. Range of messenger action of Calcium ion and inositol 1,4,5 trisphosphate. *Science.* 258:1812–1815.

81. Milner, R. E., K. S. Famulski, and M. Michalak. 1992. Calcium binding proteins in the sarco/endoplasmatic reticulum of muscle and non-muscle cells. *Mol. Cell. Biochem.* 112:1–13.

82. Wagner, J., and J. Keizer. 1994. Effects of rapid buffers on Ca^{2+} diffusion and Ca^{2+} oscillations. *Biophys. J.* 67:447–456.

83. Arecchi, F. T., and A. Politi. 1980. Transient fluctuations in the decay of an unstable state. *Phys. Rev. Lett.* 45:1219–1222.

84. Yao, Y., J. Choi, and I. Parker. 1995. Quantal puffs of intracellular Ca^{2+} evoked by inositol trisphosphate in Xenopus oocytes. *J. Physiol.* 482:533–553.

85. Dragoni, S., U. Laforenza, …, F. Moccia. 2011. Vascular endothelial growth factor stimulates endothelial colony forming cells proliferation and tubulogenesis by inducing oscillations in intracellular Ca^{2+} concentration. *Stem Cell.* 29:1898–1907.

86. Cao, P., X. Tan, …, J. Sneyd. 2014. A deterministic model predicts the properties of stochastic calcium oscillations in airway smooth muscle cells. *PLoS Comput. Biol.* 10:e1003783.

87. Lembong, J., B. Sabass, and H. A. Stone. 2017. Calcium oscillations in wounded fibroblast monolayers are spatially regulated through substrate mechanics. *Phys. Biol.* 14:045006.

88. Skupin, A., and M. Falcke. 2007. Statistical properties and information content of calcium oscillations. *Genome Inform.* 18:44–53.

89. Falcke, M., and V. N. Friedhoff. 2018. The stretch to stray on time: Resonant length of random walks in a transient. *Chaos.* 28:053117.

90. Kubo, R. 1966. Fluctuation-dissipation theorem. *Rep. Prog. Phys.* 29:255–284.

91. Lindner, B. 2004. Moments of the first passage time under external driving. *J. Stat. Phys.* 117:703–737.